



Cite this: *Mater. Adv.*, 2025,  
6, 5126

## Defect mediated modulation of electrochemical efficacy and stability of $\text{Fe}_3\text{O}_4$ nanodiamond incorporated $\text{MoS}_2$ based hierarchical 2D nanostructures for high performance supercapacitor electrodes†

Md. Raihan Siddiki,<sup>a</sup> Shahid Abubakar Abtahee,<sup>ac</sup> Mehedi Hasan,<sup>b</sup> Mizanur Rahaman,<sup>b</sup> Muhammad Rakibul Islam <sup>b</sup> and Md. Abdullah Zubair <sup>a\*</sup>

In this study, pristine  $\text{MoS}_2$  and 1 to 5 wt%  $\text{Fe}_3\text{O}_4$  nanodiamond incorporated  $\text{MoS}_2$  nanoflowers were synthesized *via* a facile hydrothermal route to identify the optimal material combination for electrodes in supercapacitors. The nanostructured composite with 3%  $\text{Fe}_3\text{O}_4$  nanodiamonds exhibited an impressive specific capacitance of  $712 \text{ F g}^{-1}$  at  $0.3 \text{ A g}^{-1}$  current density and remarkable cyclic stability, with 84% capacitance retention and 103% coulombic efficiency after 10 000 cycles at  $2 \text{ A g}^{-1}$  current density. The crystallographic and morphological analyses revealed that the improved electrochemical performance of the optimum composition could be attributed to the formation of disorder induced surface active sites and broadening of crystallographic interlayer spacing of  $\text{MoS}_2$  leading to an enhancement in ionic adsorption, intercalation and surface redox reaction. Additionally, the reduced interface charge transfer resistance for the optimal composition obtained from the EIS analysis could also contribute towards specific capacitance enhancement by facilitating the faradaic process. However, the observed diminution in capacitance by 50% above the optimum  $\text{Fe}_3\text{O}_4$  content (5%) was attributed to a sudden drop in electrolytic channel integrity. The power ( $45\text{--}90 \text{ W kg}^{-1}$ ) and energy ( $2.15\text{--}3.70 \text{ W h kg}^{-1}$ ) densities of the material obtained from the two-electrode system setup corresponded to the performance zone of symmetric supercapacitors in the Ragone plot. These findings highlight the  $\text{Fe}_3\text{O}_4$  nanodiamond incorporated  $\text{MoS}_2$  nanocomposite as a very effective material for high performance supercapacitors, noticeably out-performing other material combinations with different morphologies.

Received 30th March 2025,  
Accepted 11th June 2025

DOI: 10.1039/d5ma00291e

[rsc.li/materials-advances](http://rsc.li/materials-advances)

## Introduction

The demand for energy storage and energy conversion from renewable sources is of great concern due to the rapid development of human civilization and the growing global economy. Proper utilization of renewable energy sources like the sun, wind, water, and others provides an apparent solution towards remediation of contemporary energy crisis and environmental pollution.<sup>1,2</sup> Nevertheless, solar energy availability varies

significantly with the time of day, weather conditions, and seasonal changes, making it challenging to rely on it solely for continuous power supply. Wind power is also unpredictable due to fluctuating wind speeds, which vary with weather patterns and geographical location, leading to inconsistent power output from wind turbines. The inconsistency and the unpredictable nature of these resources throughout the entire time period create a substantial obstruction towards their usability and thus cannot fully address our needs. Therefore, to secure a long-term sustainable energy future, it is essential not only to rely on renewable sources but also to find alternative ways to incorporate cutting-edge technologies for energy storage, such as fuel cells, batteries, and supercapacitors (SCs).<sup>3–5</sup> Among the numerous alternatives, a novel type of electrochemical capacitor called supercapacitors have attracted significant research attention as a promising energy storage device. This is due to their enhanced power density, safety, high charge-discharge rates, superior cycle stability, extended life

<sup>a</sup> Department of Nanomaterials and Ceramic Engineering, Bangladesh University of Engineering and Technology, Dhaka, Bangladesh.

E-mail: [mazubair2017@gmail.com](mailto:mazubair2017@gmail.com)

<sup>b</sup> Department of Physics, Bangladesh University of Engineering and Technology, Dhaka, Bangladesh

<sup>c</sup> Mechanical Engineering and Engineering Science, The University of North Carolina at Charlotte, North Carolina, USA

† Electronic supplementary information (ESI) available. See DOI: <https://doi.org/10.1039/d5ma00291e>



cycle, and the ability to operate with minimal maintenance costs at low temperatures. These advantageous characteristics of supercapacitors have drawn significant interest from both the scientific and technological sectors, recognizing them as a potential alternative for batteries.<sup>6,7</sup> As a result, supercapacitors are being widely used in various applications such as smart door locks, hybrid forklifts, cranes, smart grids, televisions, UPS (uninterruptible power supply) systems, electric vehicles, and other electronic devices.<sup>8,9</sup> However, the performance of supercapacitors relies heavily on the properties of electrode materials.

Recently, the transition metal oxides have gained attention as a promising option for developing energy storage device electrodes due to their diverse compositions, unique morphologies, larger specific surface area, and higher specific capacitance. These types of materials are crucial for enhancing the performance of supercapacitors, particularly by offering improved capacitance through nanoscale defect manipulation and surface/interface engineering. Despite these appreciable properties and potentials, challenges associated with low electrical conductivity, uncontrolled volume expansion and slow ionic diffusion often hinder their peak performance.<sup>10-13</sup> To address these issues, researchers have employed numerous strategies, such as doping, creating multi-cation structures, introducing porous architectures, and making composites. These strategies aim to help transition metal oxides overcome their inherent limitations and play a crucial role in achieving the desired goals in energy storage technologies.<sup>14-18</sup> Nowadays, nanostructured transition metal dichalcogenides (TMDs) have also attracted significant research interest as promising materials for supercapacitor electrodes due to their exceptional structural and electronic properties.<sup>19</sup> Among these, molybdenum disulfide ( $\text{MoS}_2$ ) stands out as a particularly promising candidate owing to its large surface area, enhanced hydrophilicity, high electrical conductivity, fast intrinsic ionic conductivity, exhibition of multiple oxidation states and multi-layer formation at the crystallographic scale.<sup>20-24</sup>  $\text{MoS}_2$  features a two-dimensional layered structure consisting of S-Mo-S atomic tri-layers, where molybdenum (Mo) and sulfur (S) atoms are strongly bonded by covalent bonds, and these S-Mo-S layers are held together by weak van der Waals forces. This unique structure allows for easy intercalation of ions from the electrolyte into the  $\text{MoS}_2$  interlayers without any distortion of the crystal structure.<sup>25,26</sup> The multi-valence states of Mo (+2 to +6), and the space between the interlayers supporting the intercalation of cations provide  $\text{MoS}_2$  with pseudo-capacitance properties. Nevertheless, the inherent restacking property, poor conductivity, unstable solid-electrolyte interface, and side reactions linked to electrolyte decomposition contribute to low capacitance and limited cyclic stability, potentially limiting its effectiveness as an electrode material.<sup>27-29</sup>

Numerous studies have explored the various morphologies of  $\text{MoS}_2$  nanoparticles, particularly in the context of their use in composite materials.<sup>30-36</sup>  $\text{Fe}_3\text{O}_4$  (magnetite) is frequently chosen as a complementary component for  $\text{MoS}_2$  due to its remarkable magnetic and surface characteristics. The electrical conductivity of  $\text{Fe}_3\text{O}_4$  is significantly enhanced by the presence

of multiple valence states of Fe which enables electron transition between  $\text{Fe}^{2+}$  and  $\text{Fe}^{3+}$  cations within the octahedral sites. Composite materials incorporating  $\text{Fe}_3\text{O}_4$  exhibit outstanding stability. Additionally, surface functionalization of  $\text{Fe}_3\text{O}_4$  nanoparticles further improves their stability and increases the specific surface area.<sup>37-39</sup> However iron oxide-based materials alone face inherent limitations due to their sluggish ion diffusion kinetics. Various types of nanostructures for iron oxide-based electrodes, such as spheres, buttons, microspheres, octahedra, and nanowires, have been investigated, showing notable electrochemical performance. To address the individual shortcomings of these materials, iron oxides, particularly  $\text{Fe}_3\text{O}_4$ , are often combined with  $\text{MoS}_2$  for electrochemical applications.<sup>33-36</sup> Such combinations have been found to significantly improve the electrochemical properties of the materials.

Sarno *et al.* introduced a nanostructure composed of uniformly sized  $\text{Fe}_3\text{O}_4$  nanoparticles embedded in  $\text{MoS}_2$  nanosheets, achieving a specific capacitance of  $670 \text{ F g}^{-1}$  at  $0.25 \text{ A g}^{-1}$  and 76% capacitance retention after 2000 cycles.<sup>36</sup> Bayat *et al.* investigated a  $\text{MoS}_2/\text{Fe}_3\text{O}_4/\text{PANI}$  composite, where polygon-shaped  $\text{Fe}_3\text{O}_4$  nanoparticles were dispersed on  $\text{MoS}_2$  sheets, delivering a specific capacitance of  $401 \text{ F g}^{-1}$  at  $0.5 \text{ A g}^{-1}$  and excellent cycling stability with 89.3% retention after 5000 cycles.<sup>33</sup> Salarizadeh *et al.* synthesized a ternary hybrid nanocomposite of sheet-like  $\text{MoS}_2$ , spherical  $\text{Fe}_3\text{O}_4$ , and reduced graphene oxide (rGO) *via* a two-step hydrothermal process, which yielded a high specific capacitance of  $527 \text{ F g}^{-1}$  at  $0.5 \text{ mA cm}^{-2}$  and 93% capacitance retention after 5000 cycles.<sup>34</sup> Similarly, Li *et al.* developed a ternary carbon nanotube/flower-like  $\text{MoS}_2$ /spherical  $\text{Fe}_3\text{O}_4$  nanocomposite with a specific capacitance of  $522.7 \text{ F g}^{-1}$  at  $0.5 \text{ A g}^{-1}$ , using a two-step hydrothermal method.<sup>35</sup> These studies demonstrate that the combination of  $\text{MoS}_2$  and iron oxide in a single structure shows significant promise for high-performance supercapacitor electrodes, offering benefits such as improved specific capacitance due to the high redox electroactivity of these two components and a reduced diffusion path that promotes rapid and reversible faradaic reactions.

In this study, diamond-shaped  $\text{Fe}_3\text{O}_4$  nanoparticles were incorporated into  $\text{MoS}_2$  to enhance its specific capacitance. The  $\text{MoS}_2$  particles exhibited flower-like nanostructures, formed by an assembly of numerous nanopetals in a hierarchical manner. To the best of our knowledge, the diamond-shaped  $\text{Fe}_3\text{O}_4$  nanoparticles were integrated hierarchically into  $\text{MoS}_2$  nanoflowers in this study for the first time. To evaluate the impact of  $\text{Fe}_3\text{O}_4$  nanodiamonds on the electrochemical performance of  $\text{MoS}_2$  nanoflowers, pure  $\text{MoS}_2$  and three nanocomposites of  $\text{MoS}_2$  with 1, 3 and 5 wt%  $\text{Fe}_3\text{O}_4$  denoted as  $\text{MoS}_2/(1\%) \text{ Fe}_3\text{O}_4$ ,  $\text{MoS}_2/(3\%) \text{ Fe}_3\text{O}_4$ , and  $\text{MoS}_2/(5\%) \text{ Fe}_3\text{O}_4$ , respectively, were synthesized *via* a simple hydrothermal method. The performance of these nanocomposites, along with a pure  $\text{MoS}_2$  nanoflower sample as a reference, was then evaluated electrochemically to determine the optimal  $\text{Fe}_3\text{O}_4$  content for improved electrochemical response and compared with similar nanocomposites available in the recent literature to assess the materials' usability as a high-performance supercapacitor electrode.

# Materials and methods

## Materials

Sodium molybdate dihydrate ( $\text{Na}_2\text{MoO}_4 \cdot 2\text{H}_2\text{O}$ ) and thiourea ( $\text{CH}_4\text{N}_2\text{S}$ ) were used as precursors for the synthesis of  $\text{MoS}_2$  nanoflowers. Iron(III) chloride hexahydrate ( $\text{FeCl}_3 \cdot 6\text{H}_2\text{O}$ ), polyethylene glycol (PEG 8000), and hydrazine 64% ( $\text{N}_2\text{H}_4$ ) were used to prepare  $\text{Fe}_3\text{O}_4$  nanoparticles. All reagents were obtained from Merck, India, and were of analytical grade (purity  $\geq 98\%$ ), eliminating the need for additional purification. Deionized (DI) water was used as the solvent during the synthesis processes. All required nanostructured materials were prepared by adopting a facile hydrothermal synthesis route.

### Synthesis of diamond shaped $\text{Fe}_3\text{O}_4$ nanoparticles

To synthesize diamond shaped  $\text{Fe}_3\text{O}_4$  nanoparticles, 0.028 mol of  $\text{FeCl}_3 \cdot 6\text{H}_2\text{O}$  and 0.0003 mol of PEG were dissolved by magnetic stirring in 80 mL of DI water for 30 minutes. After that, 9 mL of  $\text{N}_2\text{H}_4$  was added to the solution dropwise. When the solution color became dark brown during the addition of  $\text{N}_2\text{H}_4$ , it was immediately transferred to a Teflon-lined autoclave and heated in an oven at 160 °C for 4 hours. The resulting solution with precipitate was cooled naturally. Using DI water and ethanol, the precipitate was washed and collected by centrifuging the solution and then dried in an oven at 60 °C for 24 hours to obtain the diamond shaped  $\text{Fe}_3\text{O}_4$  nanoparticles.

### Synthesis of $\text{MoS}_2$ nanoflowers

To synthesize  $\text{MoS}_2$  nanoflowers, 0.0119 mol of  $\text{Na}_2\text{MoO}_4 \cdot 2\text{H}_2\text{O}$  was dissolved in 85 mL of deionized water and stirred vigorously until a clear solution was obtained. Subsequently, 0.05525 mol of  $\text{CH}_4\text{N}_2\text{S}$  was introduced into the solution, with continuous stirring for an additional 30 minutes to homogenize the solution. Once the homogeneity was achieved, the solution was quickly transferred to a Teflon-lined autoclave and heated at a temperature of 200 °C for 24 hours in an oven. The resultant suspension was centrifuged and washed using DI water and ethanol to collect the precipitate. The collected substance was then dried in an oven at 60 °C for 10 hours to obtain the  $\text{MoS}_2$  nanoflowers.

### Synthesis of $\text{MoS}_2$ nanoflower– $\text{Fe}_3\text{O}_4$ nanodiamond composites

To synthesize  $\text{MoS}_2$ /(1 wt%)  $\text{Fe}_3\text{O}_4$ , 0.0119 mol of  $\text{Na}_2\text{MoO}_4 \cdot 2\text{H}_2\text{O}$  and 0.05525 mol of  $\text{CH}_4\text{N}_2\text{S}$  were mixed by vigorous stirring for 30 minutes in 80 mL of deionized water. Subsequently, an appropriate quantity of pre-synthesized  $\text{Fe}_3\text{O}_4$  nanodiamonds was added into the solution and subjected to sonication using a probe sonicator for 30 minutes to ensure a homogeneous suspension. The resulting mixture was then immediately transferred to a Teflon-lined autoclave and placed in an oven, where it was heated at 200 °C for 24 hours. The resultant material was separated through centrifugation, subjected to multiple washes with ethanol and DI water, and then dried at a temperature of 60 °C for 24 hours to obtain the desired composite. Following a similar procedure, varying amounts of  $\text{Fe}_3\text{O}_4$  (3 and 5 wt%) were used to synthesize  $\text{MoS}_2$ /(3 wt%)  $\text{Fe}_3\text{O}_4$  and  $\text{MoS}_2$ /(5 wt%)  $\text{Fe}_3\text{O}_4$

nanocomposites, respectively. The synthesis process is schematically depicted in Fig. 1.

Fig. 2 schematically shows the synthesized nanoflowers of pure  $\text{MoS}_2$  and  $\text{MoS}_2/\text{Fe}_3\text{O}_4$  nanocomposites. The  $\text{MoS}_2$  nanoflowers are composed of numerous nano-sized petals. In the nanocomposites, diamond-shaped  $\text{Fe}_3\text{O}_4$  nanoparticles are embedded within the  $\text{MoS}_2$  nanoflowers. As the  $\text{Fe}_3\text{O}_4$  content increases to 5%, these nanoparticles begin to protrude from the surface of the  $\text{MoS}_2$  nanoflowers, disrupting the hierarchical growth of the flower type structures, and the nanopetals become scattered, resembling a pile of discarded petals.

## Electrode preparation

To prepare the working electrodes, the active material's slurry was applied to a 0.3  $\text{cm}^2$  specific area of a glassy carbon electrode. This slurry was prepared by mixing 96% active material with 4% polyvinyl alcohol (PVA) and dimethyl sulfoxide. The mixture was then subjected to sonication for several hours. In this method, PVA acts as a binder, containing hydroxyl groups that enable hydrogen bond formation between the glassy carbon electrode and the active material. Dimethyl sulfoxide serves as a dispersant to achieve uniform slurry, which can help produce high quality electrodes.

## Characterization

For crystallographic characterization, X-ray diffraction (XRD) patterns of the nanostructured particles (NPs) were recorded over a  $2\theta$  range of 10° to 80° using a PANalytical Empyrean diffractometer equipped with a Cu-K $\alpha$  X-ray source ( $\lambda_a = 1.54278 \text{ \AA}$ ) operated at 45 kV and 40 mA. The powder samples were placed on a silicon zero-background holder, with the surface of the sample precisely aligned with the diffraction plane. A reflection-transmission spinner module was employed to rotate the sample at a speed of 60 rpm during pattern acquisition to ensure a consistent irradiation area at both low and high X-ray incident angles. The scanning speed was set to 0.041683° per second under continuous scanning mode. A field emission scanning electron microscope (JEOL JSM 7600F) operated at 5 kV was used to examine surface morphologies. Elemental composition was analyzed by energy dispersive X-ray spectroscopy (EDX). The micromorphology of  $\text{MoS}_2/\text{Fe}_3\text{O}_4$  nanocomposites was investigated using a JEOL JEM 2100 F high-resolution transmission electron microscope (HRTEM) operated at 200 kV. For sample preparation, a small amount of ethanol was used to evenly disperse the active material, followed by 20 minutes of sonication. After sonication, the sample was placed on a carbon-coated 3 mm Cu grid and dried before being inserted into the transmission electron microscope for microstructural analysis. The electrochemical performance of electrodes consisting of pure  $\text{MoS}_2$  nanoflowers and all nanocomposites of  $\text{MoS}_2/\text{Fe}_3\text{O}_4$  was evaluated using a CS310 electrochemical workstation (Corrtest) with a three-electrode configuration, in a 0.5 M aqueous solution of  $\text{Na}_2\text{SO}_4$  as the electrolyte. The glassy carbon electrode served as the working electrode, a 1 cm  $\times$  1 cm platinum plate as the counter electrode, and  $\text{Ag}/\text{AgCl}$  as the reference electrode. The electrochemical measurements included cyclic voltammetry



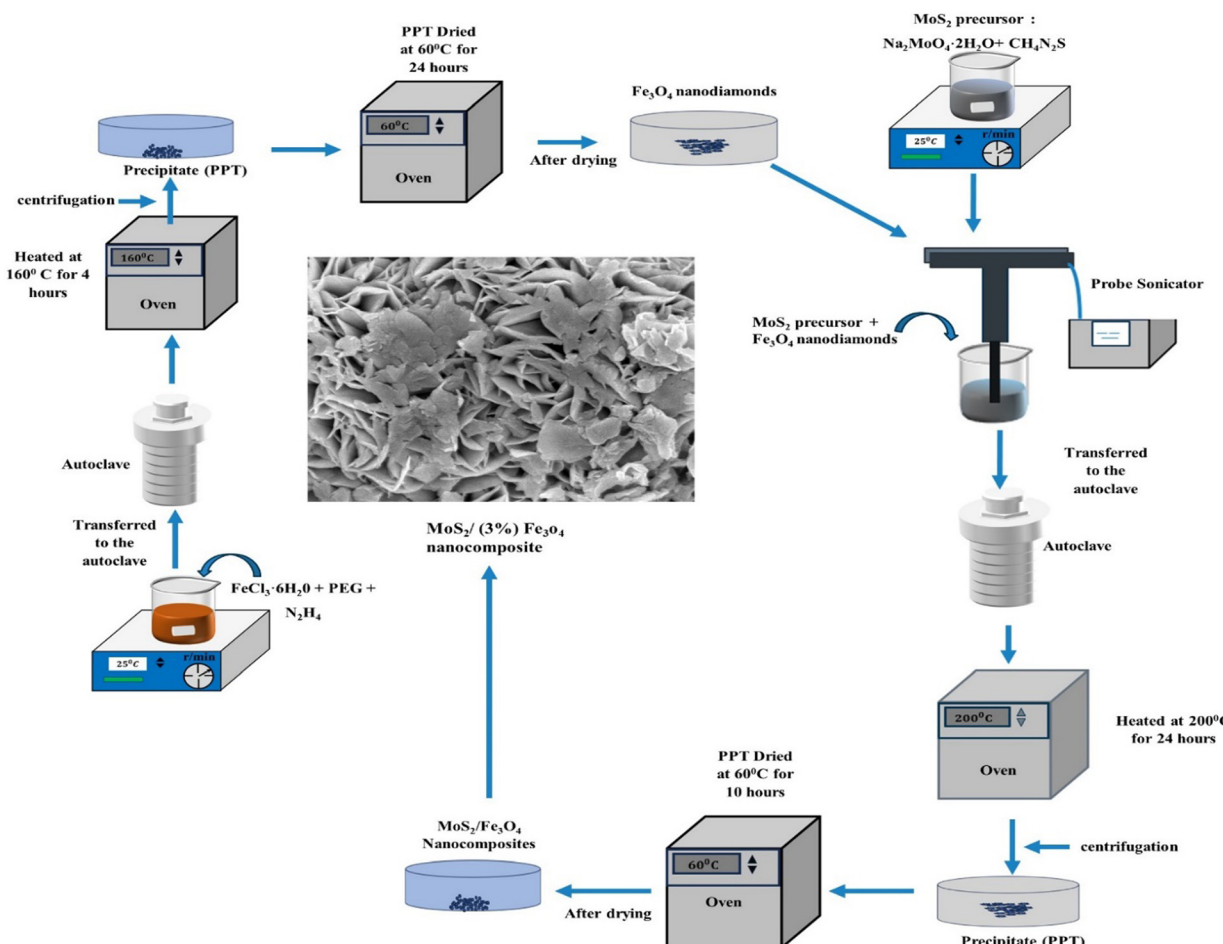


**Fig. 1** Flowchart of the synthesis process of the  $\text{MoS}_2/\text{Fe}_3\text{O}_4$  nanocomposite: after preparing diamond-shaped  $\text{Fe}_3\text{O}_4$ , it is mixed into the precursor solution of  $\text{MoS}_2$  nanoflowers in various amounts: 1%, 3%, and 5%, producing  $\text{MoS}_2/(1\%) \text{Fe}_3\text{O}_4$ ,  $\text{MoS}_2/(3\%) \text{Fe}_3\text{O}_4$  and  $\text{MoS}_2/(5\%) \text{Fe}_3\text{O}_4$  nanocomposites, respectively.

(CV), galvanostatic charge–discharge (GCD), and electrochemical impedance spectroscopic (EIS) analyses. The CV and GCD analyses were performed within a potential window of  $-0.2$  V to  $0.7$  V, with scan rates of 20, 40, 60, 80, and  $100 \text{ mV s}^{-1}$  and EIS analysis was performed using a sinusoidal bias signal over a frequency range of  $10^{-1}$  to  $10^5$  Hz. Furthermore, a symmetric two-electrode supercapacitor configuration was used to evaluate the real device performance with an optimized  $\text{MoS}_2/\text{Fe}_3\text{O}_4$  nanocomposite. To prepare the symmetric cell, a slurry of the active materials was cast on two glassy carbon electrodes, employed as the anode and the cathode of the supercapacitor. All other measurement conditions were kept unchanged for the two-electrode configuration.

## Results and discussion

### X-ray diffraction (XRD)

Fig. 3 shows the X-ray diffraction (XRD) patterns of  $\text{MoS}_2$  nanoflowers and  $\text{MoS}_2/\text{Fe}_3\text{O}_4$  nanocomposites. The diffraction patterns observed for the pristine  $\text{MoS}_2$  nanoflower can be satisfactorily matched with the JCPDS card number 37-1492

and the corresponding peaks can be indexed to the (002), (100), (102), (006), and (110) reflections. The most prominent peak in the hexagonal  $\text{MoS}_2$  structure, attributed to the reflection from the (002) plane, stipulates a regular periodicity along the *c*-axis, indicating a well-layered structure along the [001] direction.<sup>40–42</sup>

In the case of  $\text{MoS}_2/\text{Fe}_3\text{O}_4$  composites with up to 3%  $\text{Fe}_3\text{O}_4$  content, no distinct  $\text{Fe}_3\text{O}_4$  peak was observed in the diffraction pattern which could likely be due to the presence of only a minute amount of  $\text{Fe}_3\text{O}_4$  nanodiamonds along with their poor crystallinity. However, a new peak at a  $2\theta$  value of  $36^\circ$  (marked with an asterisk (\*)) appeared in the diffraction pattern of the  $\text{MoS}_2/5\% \text{Fe}_3\text{O}_4$  nanocomposite which corresponded to  $\text{Fe}_3\text{O}_4$  nanodiamonds and this peak can be indexed to the (311) reflection of diamond-shaped  $\text{Fe}_3\text{O}_4$  nanoparticles, which has the highest relative intensity among all the (*hkl*) reflections from polycrystalline  $\text{Fe}_3\text{O}_4$ .<sup>43</sup> The addition of  $\text{Fe}_3\text{O}_4$  nanodiamonds to  $\text{MoS}_2$  results in a small peak shift, observed for the (002) reflection in Fig. 3, suggesting a small uniform parent lattice deformation, which could possibly be explained by the formation of defects due to the incorporation of  $\text{Fe}^{2+}/\text{Fe}^{3+}$  ions into the  $\text{MoS}_2$  lattice. In fact, the incorporation of  $\text{Fe}_3\text{O}_4$



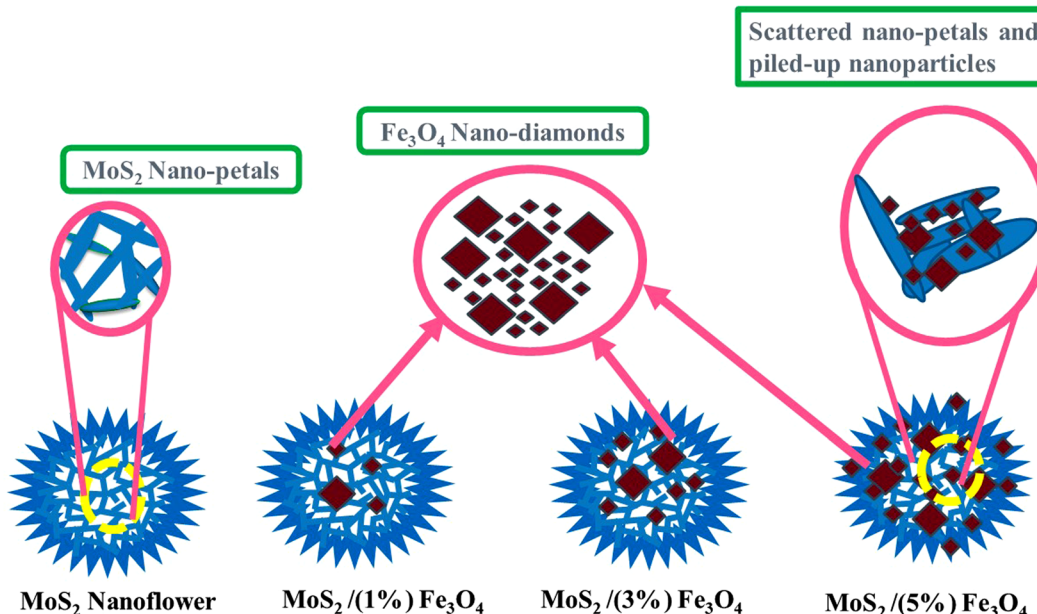
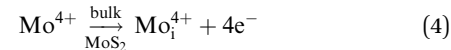
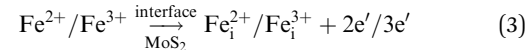
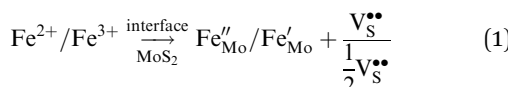
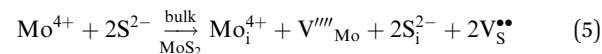


Fig. 2 The schematic illustration shows the synthesized pure  $\text{MoS}_2$  and  $\text{MoS}_2/\text{Fe}_3\text{O}_4$  nanocomposites. The  $\text{MoS}_2$  nanoflowers are composed of numerous nano-petals that are radially aligned and hierarchically grown.  $\text{Fe}_3\text{O}_4$  nanoparticles vary in size. Larger  $\text{Fe}_3\text{O}_4$  nano-diamonds protrude from the surface of the  $\text{MoS}_2$  nanoflowers due to the presence of an excessive amount of  $\text{Fe}_3\text{O}_4$ , which disrupts the formation of nano-petals and the flowers appear fragmented, resembling a disordered pile of nanopetals.

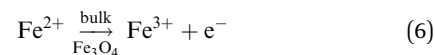
nanodiamonds into  $\text{MoS}_2$  nanoflowers could cause both  $\text{Fe}^{2+}/\text{Fe}^{3+}$  and  $\text{Mo}^{4+}$  ions to migrate across the  $\text{MoS}_2/\text{Fe}_3\text{O}_4$  interface over a limited distance (due to low ionic mobility in solid phases at low processing temperature) on either side of the interface leading to the formation of crystal defects as follows:



On top of that, in the case of material processing carried out at low temperature ( $\sim 200$  °C) the formation of bulk lattice defects within the matrix is not unlikely as shown below:



The limited migration of  $\text{Mo}^{4+}$  and  $\text{Fe}^{2+}/\text{Fe}^{3+}$  ions across the interface could create both substitutional (eqn (1) and (2)) and interstitial (eqn (3) and (4)) defects which are accompanied by generation of free carriers ( $e^-$ ) to maintain the charge neutrality within a narrow region of the interface giving rise to carrier rich zones around the contact areas between the two solid phases of the nanocomposite. Additionally, the possible coexistence of multivalence state of Fe in magnetite could contribute towards polaronic type hopping within the bulk of nanodiamonds as follows:



Apart from the above, due to the relative abundance of S with respect to Mo in the starting  $\text{MoS}_2$  precursor solution, it is

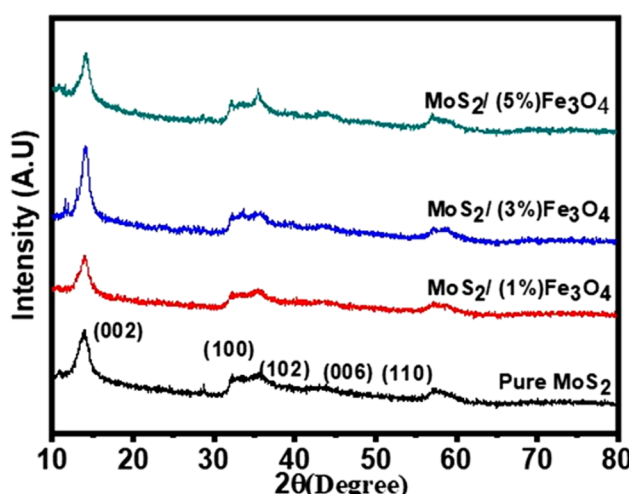


Fig. 3 XRD patterns of pure  $\text{MoS}_2$  nanoflowers and  $\text{MoS}_2/\text{Fe}_3\text{O}_4$  nanocomposites. The peak marked with an asterisk corresponds to the (311) plane of  $\text{Fe}_3\text{O}_4$  nanodiamonds, and this peak appears only in the nanocomposite with 5%  $\text{Fe}_3\text{O}_4$  due to the presence of an excessive amount of  $\text{Fe}_3\text{O}_4$ .



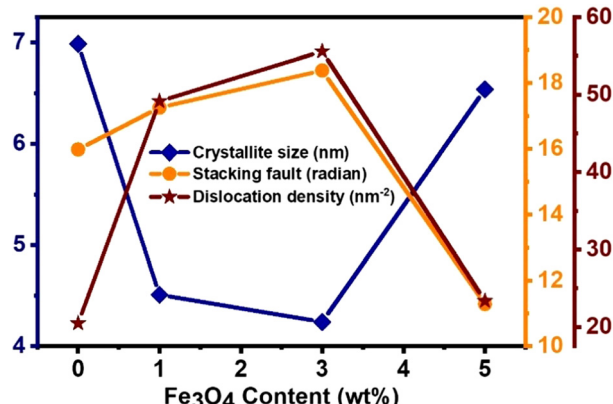


Fig. 4 The variations in crystallite size ( $L$ ), dislocation density ( $\delta$ ), and stacking fault (SF) for pure MoS<sub>2</sub> nanoflowers and  $\delta$ -MoS<sub>2</sub>/Fe<sub>3</sub>O<sub>4</sub> nanocomposites with Fe<sub>3</sub>O<sub>4</sub> content, obtained from XRD line profile analysis. The addition of 3% Fe<sub>3</sub>O<sub>4</sub> nanodiamonds resulted in the highest dislocation density and stacking fault and the smallest crystallite size.

not unlikely to expect an abundance of S-interstitial compared to any cationic interstitial within the MoS<sub>2</sub> lattice.

Now the vacancies and interstitials from reactions (1), (3) and (4) could contribute to matrix lattice distortion. The formation of defects could also generate both non-uniform and uniform lattice strain in the material, potentially leading to a reduction in the average crystallite size.<sup>44</sup> This decrease in size is also evident with the addition of Fe<sub>3</sub>O<sub>4</sub> nanodiamonds, as illustrated in Fig. 4. Nonetheless, Mo<sup>4+</sup> could also migrate across the composite interface and could form the crystallographic defects within the dispersed Fe<sub>3</sub>O<sub>4</sub> nanodiamonds as shown by eqn (2). However, with the volume fraction of the nanodiamonds being much smaller than that of the MoS<sub>2</sub> matrix, any influence of lattice disorder generated within the relatively small fraction of Fe<sub>3</sub>O<sub>4</sub> on the overall microstructure of the bulk nanostructured composite could be neglected for the time being. Yet the cationic vacancy V<sup>'''</sup><sub>Mo</sub> generated by Mo<sup>4+</sup> migration across the interface could add to defect induced disorder within the MoS<sub>2</sub> matrix lattice.

Wu *et al.* hydrothermally synthesized MoS<sub>2</sub> microspheres with a flower-like structure, where high-resolution XPS spectra revealed two core-level Mo 3d peaks at binding energies (BEs) of 229.6 eV and 232.8 eV, corresponding to Mo 3d<sub>5/2</sub> and Mo 3d<sub>3/2</sub>, characteristic of Mo(IV). Furthermore, the core-level S 2p spectra at BEs of 162.4 eV and 163.5 eV were attributed to S 2p<sub>3/2</sub> and S 2p<sub>1/2</sub>, consistent with sulfur in the -2 oxidation state.<sup>45</sup> Similarly, Li *et al.* prepared defect-rich MoS<sub>2</sub> nanoflowers by a hydrothermal method and identified BEs at 229.1 eV and 232.1 eV in the Mo 3d region, also indicative of Mo(IV). Additionally, S 2p spectral peaks with BEs of 162.3 eV and 163.5 eV were associated with S 2p<sub>3/2</sub> and S 2p<sub>1/2</sub>, confirming the S<sup>2-</sup> oxidation state.<sup>46</sup> Mizanur *et al.* developed a MoS<sub>2</sub>/MnS nanocomposite, with high-resolution XPS spectra showing six distinct peaks, including two doublets for Mo at 229 eV and 232.15 eV, confirming the presence of Mo(IV).<sup>32</sup> Pawar *et al.* analyzed Fe<sub>3</sub>O<sub>4</sub> using XPS, revealing that the Fe 2p<sub>3/2</sub> peak consisted of two maxima at 710.96 eV and 708.39 eV, whereas

the Fe 2p<sub>1/2</sub> peak was deconvoluted into peaks at 722.8 eV and 725.3 eV, indicative of the presence of Fe<sup>2+</sup> and Fe<sup>3+</sup> species.<sup>47</sup> Similarly, Esfandiari *et al.* studied the core-level XPS spectra of Fe<sub>3</sub>O<sub>4</sub>, identifying Fe(III) 2p<sub>3/2</sub> and Fe(III) 2p<sub>1/2</sub> peaks at 711.89 eV and 725.53 eV, and Fe(II) 2p<sub>3/2</sub> and Fe(II) 2p<sub>1/2</sub> peaks at 710.94 eV and 723.33 eV, respectively, confirming the coexistence of Fe<sup>2+</sup> and Fe<sup>3+</sup> in Fe<sub>3</sub>O<sub>4</sub>.<sup>48</sup>

The diffraction patterns in Fig. 3 display a significantly high noise-to-signal ratio. The presence of weak and diffuse XRD peaks suggests that the synthesized MoS<sub>2</sub> nanostructure has poor crystallinity. In such materials, the arrangement of atoms or molecules lacks long-range order, resulting in significant disorder over large scales. This poor crystallinity may be due to the factors such as the size effect, lattice distortion, dislocation density, and stacking faults that are directly connected to the formation of lattice defects.<sup>49</sup> The average crystallite size ( $L$ ) of the sample was determined using the Scherrer formula:

$$L = \frac{0.94\lambda}{\beta \cos \theta} \quad (7)$$

where  $\lambda$  is the wavelength of the X-ray used,  $\theta$  the incident angle for an  $(hkl)$  reflection and  $\beta$  the instrument corrected full-width at half-maximum of the diffraction peak. Dislocation density ( $\delta$ ) of the MoS<sub>2</sub>/Fe<sub>3</sub>O<sub>4</sub> composites was calculated using the following equation:

$$\delta = \frac{1}{L^2} \quad (8)$$

The stacking fault (SF) within the MoS<sub>2</sub> layered structure was estimated from the equation below:

$$SF = \left[ \frac{2\pi^2}{45(3 \tan \theta)^2} \right] \beta \quad (9)$$

Fig. 4 depicts the relationship between the structural parameters and the amount of diamond-shaped Fe<sub>3</sub>O<sub>4</sub> nanoparticles in MoS<sub>2</sub> nanoflowers. The addition of Fe<sub>3</sub>O<sub>4</sub> nanodiamonds results in an initial decrease in the average crystallite size by ~39% for up to 3% Fe<sub>3</sub>O<sub>4</sub> in the nanocomposite when compared to pristine MoS<sub>2</sub>. However, as the Fe<sub>3</sub>O<sub>4</sub> content exceeds 3%, the average crystallite size increases by ~54% at 5% Fe<sub>3</sub>O<sub>4</sub> relative to the crystallite size observed for 3% Fe<sub>3</sub>O<sub>4</sub> content. Additionally, Fig. 4 illustrates a variation in the stacking fault, which reflects the degree of lattice imperfections caused by the incorporation of diamond-shaped Fe<sub>3</sub>O<sub>4</sub> nanoparticles into the MoS<sub>2</sub> nanoflowers. The stacking fault exhibits ~17% increment with the increase in Fe<sub>3</sub>O<sub>4</sub> content up to 3% compared to pure MoS<sub>2</sub>. The increased stacking fault may result from crystal imperfections, vacancies, and dislocations within the layered structure. However, increasing the diamond-shaped Fe<sub>3</sub>O<sub>4</sub> content beyond 3% caused a ~39% decrease in the stacking fault for the nanocomposite with 5% Fe<sub>3</sub>O<sub>4</sub>, which at the same time led to an increase in the average crystallite size. Fig. 4 also shows the variation in interface dislocation density caused by the incorporation of diamond-shaped Fe<sub>3</sub>O<sub>4</sub> nanoparticles. The dislocation density, reflecting the level of defects arising from

lattice mismatch at the crystallite interfaces, increased by  $\sim 15\%$  for up to 3%  $\text{Fe}_3\text{O}_4$  nanodiamonds. However, it decreased by  $\sim 63\%$  for 5%  $\text{Fe}_3\text{O}_4$  incorporation compared to the  $\text{MoS}_2/(3\%) \text{Fe}_3\text{O}_4$  nanocomposite. The dislocation density and stacking fault generally indicate the level of imperfections in the prepared samples. In Fig. 4, both dislocation density and stacking fault of the  $\text{MoS}_2/\text{Fe}_3\text{O}_4$  nanocomposites appear to follow a similar trend, indirectly suggesting their interdependency. Thus, the incorporation of  $\text{Fe}_3\text{O}_4$  nanodiamonds into pure  $\text{MoS}_2$  nano-flowers causes lattice distortion, resulting in defects like dislocations, stacking imperfections, and point defects as described before, potentially leading to the formation of openings and/or interconnected channels for transportation of various charged species from the electrode surface to the interior. This could enhance the transportation of electrons and ions within the electrode. Additionally, structural imperfections within  $\text{MoS}_2$  crystals may disrupt the crystal lattice arrangement, creating new active sites that enhance electrochemical performance. The combined effects of changes in crystallite size, lattice distortion, and crystal defects can lead to increased effective surface area through the creation of new active sites, and improved charge carrier intercalation/deintercalation kinetics during the charging/discharging process.<sup>38,39,50–52</sup> Notably, among all the samples, the  $\text{MoS}_2/(3\%) \text{Fe}_3\text{O}_4$  composite shows the smallest crystallite size and the highest crystal imperfection, which are likely to contribute to improved charge carrier transportation, enhancing the overall electrochemical performance.<sup>50,53</sup>

### Scanning electron microscopy (SEM)

Fig. 5(a) shows an FE-SEM micrograph of  $\text{Fe}_3\text{O}_4$  nanoparticles. Due to their diamond-like appearance, these  $\text{Fe}_3\text{O}_4$  nanoparticles are referred to as nano-diamonds, as illustrated in

the inset of Fig. 5(a). The  $\text{Fe}_3\text{O}_4$  particles display two distinct size distributions, where more than 80% of the particles are  $\sim 40\text{--}50\text{ nm}$  in size, while the larger particles, making up less than 20% of the total, range from  $\sim 300$  to  $400\text{ nm}$ . Fig. 5(b) and (c) display micrographs of pristine  $\text{MoS}_2$  at different magnifications, revealing a flower-like nanostructure composed of numerous aligned but curled nano-petals. These nano-petals are connected in a hierarchical fashion through a common central core (shown later), forming flower-like structures. A nanostructure typically refers to an organized formation of nanoscale sub-units, and in this case, the 2D nano-petals are arranged in a manner so as to create 3D flower-like patterns.<sup>54</sup> However, as observed in Fig. 5(b), these flower-like structures tend to form in clusters. The average diameter of the nano-structured flowers is  $\sim 5$  to  $7\text{ }\mu\text{m}$ , while the average thickness of the nano-petals is  $\sim 18\text{ nm}$ . When  $\text{Fe}_3\text{O}_4$  nanodiamonds are added to the  $\text{MoS}_2$  precursor solution,  $\text{Mo}^{4+}$  ions from the cationic precursor are likely to be drawn to the surface of the  $\text{Fe}_3\text{O}_4$  nanodiamonds due to various forces arising from van der Waals, cohesive, electrostatic, or other chemical interactions.<sup>55</sup> Negatively charged sulfide ions ( $\text{S}^{2-}$ ) from the precursor react with molybdenum ions ( $\text{Mo}^{4+}$ ) on the surface of the  $\text{Fe}_3\text{O}_4$  nanodiamonds, resulting in the formation of  $\text{MoS}_2$  nanoflowers.

The 3D porous architecture of the nanoflower includes both micro-pores (larger pores) and nano-pores (smaller pores). Micropores provide pathways for the rapid transport of electrolyte ions, while nano-pores offer a large surface area for ion storage and electrochemical reactions. This hierarchical porous structure ensures easy access of ions from the bulk electrolyte to the active sites within the material, which is essential for high-performance energy storage devices.<sup>56,57</sup> In these applications, electrochemical reactions depend on the active sites on

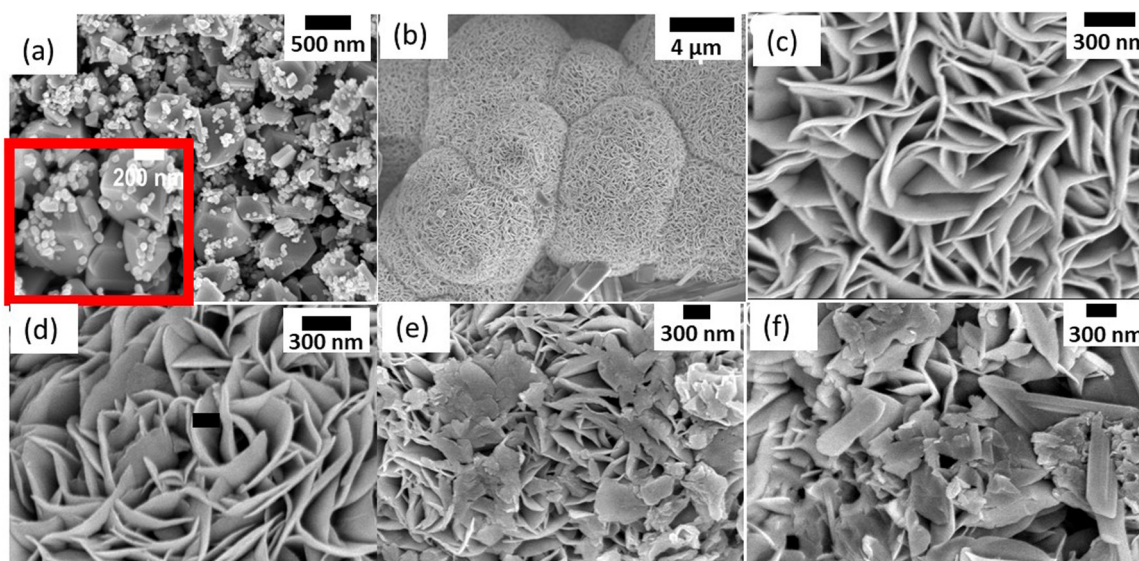


Fig. 5 FE-SEM micrographs of (a)  $\text{Fe}_3\text{O}_4$  nanodiamonds, (b and c) pristine  $\text{MoS}_2$  nanoflowers at different magnifications where the nanopetals are grown in a hierarchical manner, (d)  $\text{MoS}_2/(1\%) \text{Fe}_3\text{O}_4$  nanocomposite, (e)  $\text{MoS}_2/(3\%) \text{Fe}_3\text{O}_4$  nanocomposite, and (f)  $\text{MoS}_2/(5\%) \text{Fe}_3\text{O}_4$  nanocomposite. The micrographs of the  $\text{MoS}_2/(1\%) \text{Fe}_3\text{O}_4$  and  $\text{MoS}_2/(3\%) \text{Fe}_3\text{O}_4$  nanocomposites look similar to pristine  $\text{MoS}_2$  nanoflowers due to low  $\text{Fe}_3\text{O}_4$  content. When  $\text{Fe}_3\text{O}_4$  content exceeds 3%, the nanodiamonds protrude from the surface of the  $\text{MoS}_2$  nanoflowers causing the nanoflowers to become fragmented, and thus giving them the appearance of randomly piled up nanopetals.



the material's surface to achieve better redox capacity and faster mass transfer rates. The porous architecture arising from the nanoflower-like structure of  $\text{MoS}_2$  increases the material's specific surface area. A higher specific surface area means more active sites are available for electrochemical reactions, which directly contributes to larger capacitance and better energy storage capabilities.<sup>58,59</sup>

$\text{Na}^+$  ions can be intercalated or extracted not only at the surface but also within the pores due to the nanoporous structure of  $\text{MoS}_2$  that allows efficient penetration of the electrolyte. The unique morphology of the  $\text{MoS}_2$  nanoflowers consists of structural imperfections, such as dislocations, stacking faults and point defects within the  $\text{MoS}_2$  nanoflowers, creating additional pathways for  $\text{Na}^+$  ion diffusion. These imperfections reduce the energy barrier for ion movement, allowing ions to travel more freely through the electrode material. Besides, the nanoflower morphology improves the contact between the electrode material and the electrolyte. Better interfacial contact ensures efficient ion exchange and minimizes the resistance at the electrode-electrolyte interface.<sup>60,61</sup> Fig. 5(d) displays the micrograph of the  $\text{MoS}_2$ /(1%)  $\text{Fe}_3\text{O}_4$  nanocomposite. Due to the low wt% of  $\text{Fe}_3\text{O}_4$ , the micrograph closely resembles that of pristine  $\text{MoS}_2$  nanoflowers. However, the average thickness of the nano-petals has slightly increased to  $\sim 21$  nm. The  $\text{MoS}_2$  nanoflowers maintain their structure without any noticeable disruption in nano-petal orientation, even with a higher  $\text{Fe}_3\text{O}_4$  content (3%), as shown in Fig. 5(e). Additionally, the average thickness of the

nano-petals increases to  $\sim 26$  nm at 3%  $\text{Fe}_3\text{O}_4$  content. As can be seen from Fig. 5(d) and (e), the  $\text{Fe}_3\text{O}_4$  nanodiamonds are barely noticeable for up to 3 wt%  $\text{Fe}_3\text{O}_4$ , whereas from Fig. 5(f), it can be found that as the amount of  $\text{Fe}_3\text{O}_4$  nanodiamonds increases to 5%, some of their larger particles are observed to protrude on the surface of the  $\text{MoS}_2$  nanoflowers. This hinders the uninterrupted growth of the nano-petals, leading to noticeable disruptions in both the bulk and the surface regions. Consequently, the nanoflowers become fragmented, giving the appearance of randomly scattered pile of discarded petals, as depicted in Fig. 5(f). Here the growth of the nano-petals is uneven, with some growing excessively compared to others, resulting in significant variation in thickness, ranging from  $\sim 18$  to  $37$  nm. The variation of petal thickness is shown in Fig. SF3 (ESI<sup>†</sup>).

The typical standardless EDX (area analysis) semiquantitative spectral analysis in Fig. SF1 (ESI<sup>†</sup>) illustrates the variation in S/Mo atomic % ratio with the incorporation of  $\text{Fe}_3\text{O}_4$  nanodiamonds, as clearly depicted in Fig. SF2 (ESI<sup>†</sup>). This ratio appears to increase from  $\sim 7.4$  to  $\sim 13.3$  with the addition of  $\text{Fe}_3\text{O}_4$  up to 5 wt%, qualitatively indicating an abundance of the S atom in  $\text{MoS}_2$  nanoflowers. Such plenitude of sulfur could be accommodated as interstitial defects within  $\text{MoS}_2$  lattice planes as discussed earlier, and concurrently, a possible accumulation of sulfur atoms on the surface of  $\text{MoS}_2$  nanopetals cannot be ignored as suggested by Wu *et al.*<sup>45</sup> It may further be inferred that this superficial accumulation of abundant unsaturated sulfur atoms could occur from the presence of an ample

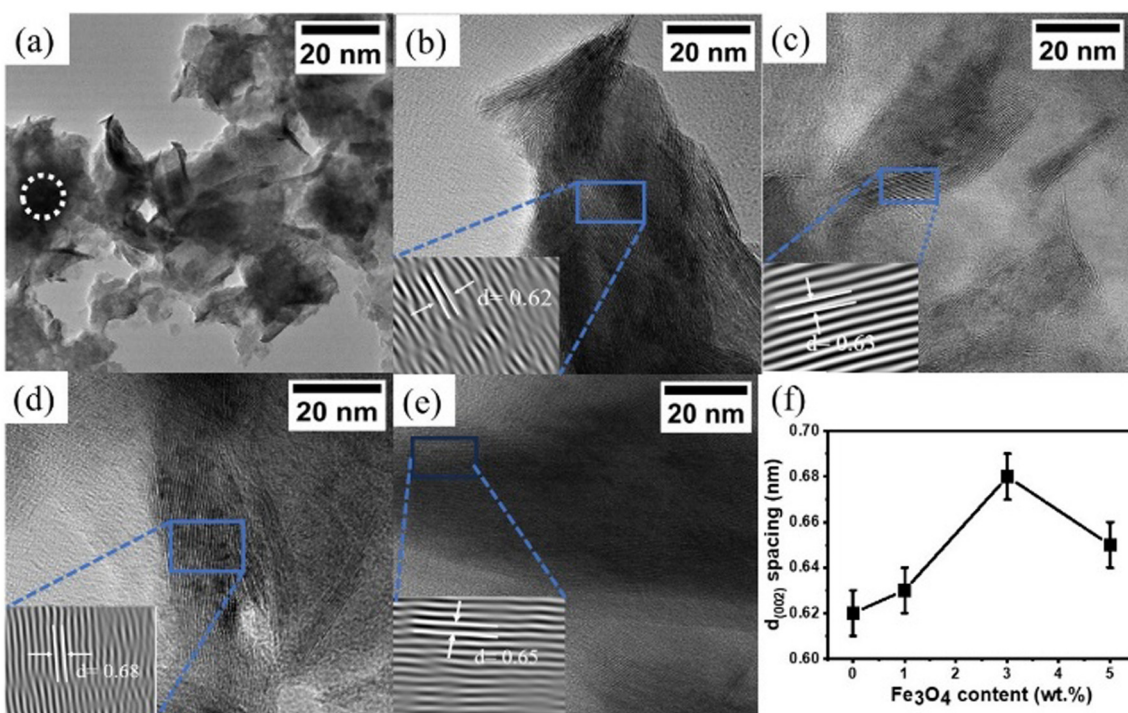


Fig. 6 (a) TEM image of  $\text{MoS}_2$  nanoflowers. HR-TEM images of (b) pure  $\text{MoS}_2$ , (c)  $\text{MoS}_2$ /(1%)  $\text{Fe}_3\text{O}_4$ , (d)  $\text{MoS}_2$ /(3%)  $\text{Fe}_3\text{O}_4$ , and (e)  $\text{MoS}_2$ /(5%)  $\text{Fe}_3\text{O}_4$ . (f) Variation of  $d$ -spacing as a function of  $\text{Fe}_3\text{O}_4$  content. Here, the generation of defects due to the possible incorporation of Fe ions into the  $\text{MoS}_2$  lattice leads to the augmentation of interplanar spacing. Other point defects like S-interstitials and vacant sites could also contribute to enhancing the interplanar spacing.



number of defects on the surface of ultra-thin nanosheets of  $\text{MoS}_2$ , enhancing the stability of the nano petals of  $\text{MoS}_2$  through decreasing their surface energies.<sup>62,63</sup> These active unsaturated atoms may also affect the electronic structure and modulate the activity of the reactive sites which ultimately influences the electrochemical properties.<sup>64</sup>

### Transmission electron microscopy (TEM)

Fig. 6(a) presents the transmission electron microscopic (TEM) image of pure  $\text{MoS}_2$  nanoflowers, which consist of numerous nano-petals stacked in a hierarchical manner. These petal-like nanostructures appear to emerge from the core of the nanoflower (indicated by a dotted circle in Fig. 6(a)) extending in a radially outward direction. The nano-petals overlap with each other at some point due to their curled, wrinkled structures and are exceptionally thin with slightly varying thicknesses and partially transparent, as indicated by the varying light contrasts in different areas. The HRTEM image in Fig. 6(b) displays the disordered lattice fringes of  $\text{MoS}_2$  nanoflowers, with a lattice spacing of  $\sim 0.62$  nm corresponding to the (002) plane of the hexagonal structure, consistent with JCPDS card no. 37-1492, and the observed (002) plane of hexagonal  $\text{MoS}_2$  further suggests the growth of hexagonal nanopetals along the [002] crystal axis.<sup>30</sup> The HRTEM images of the nanocomposites, shown in Fig. 6(c–e), reveal discontinuities in the lattice fringes at the curled edges, indicating the presence of dislocations and imperfections in the stacking sequence.<sup>40,45</sup> The lattice spacings corresponding to the (002) planes of  $\text{MoS}_2$  are observed to be  $\sim 0.63$  nm,  $\sim 0.68$  nm, and  $\sim 0.65$  nm for 1%, 3% and 5%  $\text{Fe}_3\text{O}_4$ , respectively. This suggests that the addition of  $\text{Fe}_3\text{O}_4$  nanoparticles to the  $\text{MoS}_2$  nanoflower significantly increases the lattice spacing of the nanocomposites, as illustrated in Fig. 6(f). The incorporation of  $\text{Fe}_3\text{O}_4$  nanoparticles into the  $\text{MoS}_2$  nanoflowers can create defects within the  $\text{MoS}_2$  lattice as described before, leading to an enhancement in interplanar gaps.<sup>65</sup> Furthermore, the observation of expanded lattice fringes may also suggest the presence of crystal defects, forming along crystal boundaries as a result of strain relief. Such defects may provide accessible storage sites, shortening the path for electrolyte ions. Additionally, the slight broadening of interlayer spacing can help prevent the crystallographic layers from collapsing during fast charge–discharge cycles. The hydrothermally produced  $\text{MoS}_2/\text{Fe}_3\text{O}_4$  nanocomposite, with its nanoporous surface, widened interlayer spacing, and unique nanoflower–nanodiamond morphology, can lead to an augmentation in specific capacitance by providing better ion intercalation, more electroactive sites, and improved electrolyte access, resulting in superior electrochemical properties and higher efficiency.<sup>55,66,67</sup>

The TEM EDX spectra of the  $\text{MoS}_2$  and  $\text{MoS}_2/\text{Fe}_3\text{O}_4$  nanostructured materials are shown in Fig. SF4(a–d) (ESI†). In Fig. SF4(a) (ESI†), the peaks corresponding to Mo and S elements come from pure  $\text{MoS}_2$ . In Fig. SF4(b) (ESI†), no Fe peak is observed for the  $\text{MoS}_2/(1\%) \text{Fe}_3\text{O}_4$  nanocomposite, which can be attributed to the very small amount of  $\text{Fe}_3\text{O}_4$  being added to  $\text{MoS}_2$ . When 3%  $\text{Fe}_3\text{O}_4$  nanodiamonds are incorporated into  $\text{MoS}_2$ , a small Fe peak becomes noticeable in the EDX spectrum

as shown in Fig. SF4(c) (ESI†), suggesting the presence of  $\text{Fe}_3\text{O}_4$  nanodiamonds. However, Fig. SF4(d) (ESI†) exhibits a prominent peak of Fe in the  $\text{MoS}_2/(5\%) \text{Fe}_3\text{O}_4$  nanocomposite due to a higher amount of  $\text{Fe}_3\text{O}_4$  incorporation.

### Electrochemical performance analysis

**Cyclic voltammetry (CV).** Cyclic voltammetry (CV) was performed to examine the charge storage mechanism of pristine  $\text{MoS}_2$  and diamond-shaped  $\text{Fe}_3\text{O}_4$  incorporated  $\text{MoS}_2$  nanocomposites. Fig. 7(a) presents the CV loops of all the nanostructured samples for a fixed scan rate of  $60$  mV s<sup>−1</sup>. The variation of the area enclosed by these CV loops with  $\text{Fe}_3\text{O}_4$  content is shown in Fig. 7(b). The results clearly show that the CV area increases with the addition of  $\text{Fe}_3\text{O}_4$  nanodiamonds, with the  $\text{MoS}_2/(3\%) \text{Fe}_3\text{O}_4$  nanocomposite exhibiting the largest area. This enhancement in area suggests that the inclusion of  $\text{Fe}_3\text{O}_4$  nanodiamonds significantly improves the specific capacitance of  $\text{MoS}_2$  nanoflowers.<sup>68</sup> However, when the amount of  $\text{Fe}_3\text{O}_4$  nanodiamonds is raised to 5%, a reduction in the CV loop area is observed, indicating a qualitative decline in the specific capacitance of  $\text{MoS}_2$ . Such capacitance deterioration is likely to be due to the fact that at higher  $\text{Fe}_3\text{O}_4$  content ( $\sim 5\%$ ), some  $\text{Fe}_3\text{O}_4$  nanodiamonds protrude from the surface of the  $\text{MoS}_2$  nanoflowers, as depicted in Fig. 5(f), disrupting the formation of nanoflowers. As a result, the flower petals in these regions become fragmented, and piled-up in a disordered manner, causing the surface nanoporous channels for the electrolyte to collapse leading to clogging of electrolyte flow paths within the materials. Thus, the effective surface area of the  $\text{MoS}_2$  nanoflowers decreases, culminating in a reduction in specific capacitance.

Moreover, Fig. 7(c) shows additional CV measurements carried out on the  $\text{MoS}_2/(3\%) \text{Fe}_3\text{O}_4$  nanocomposite at different scan rates, knowing that this composite demonstrates the best performance. The CV curves consistently exhibit a quasi-rectangular shape at all scan rates, suggesting that both electric double-layer capacitance (EDLC) and pseudocapacitance mechanisms are likely to contribute to the charge storage process.<sup>69</sup> This observation is further validated by analyzing the slope of the Tafel plot, according to which the relationship between current and scan rate can be described by the following equation:

$$i = av^b \quad (10)$$

where  $i$  is the working electrode current density,  $v$  the scan rate, and  $b$  the Tafel slope. To determine the slope “ $b$ ”,  $\log i$  can be plotted against  $\log v$ , which should ideally give a straight line with a slope “ $b$ ” according to eqn (10) and the value of  $b$  indicates different charge storage mechanisms. Here,  $b = 0.5$  indicates a diffusion-controlled process typically associated with redox reactions where charge transfer occurs across the electrode/electrolyte interface, known as the faradaic process, and gives rise to pseudocapacitance, and  $b = 1$  represents electric double-layer capacitance (EDLC), indicating capacitive behavior with charge stored at the electrode/electrolyte interface. Values within the range  $0.5 < b < 1$  signify a combination

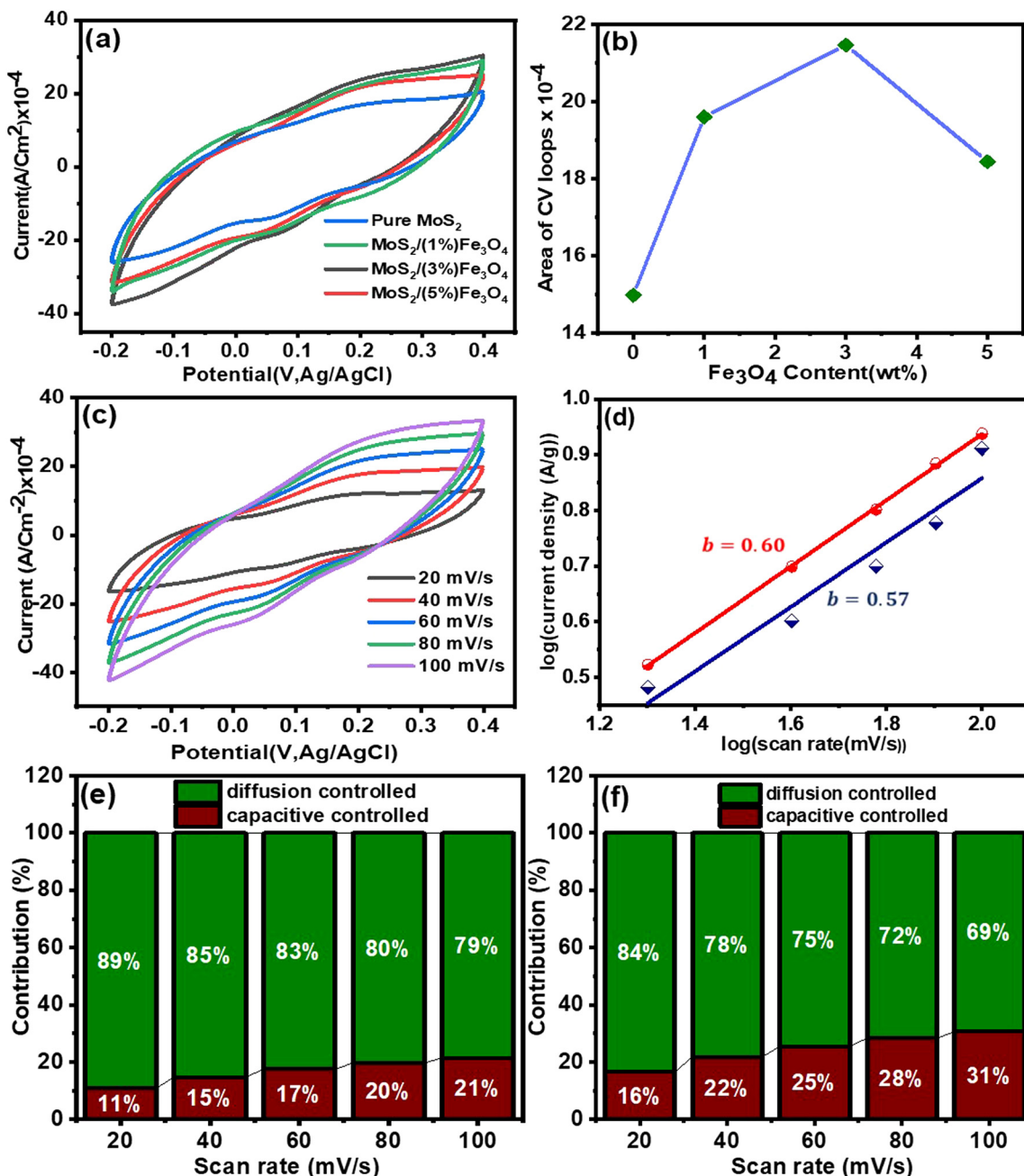


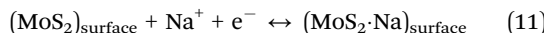
**Fig. 7** (a) CV loops of MoS<sub>2</sub> nanoflowers and other MoS<sub>2</sub>/Fe<sub>3</sub>O<sub>4</sub> nanocomposites obtained at 60 mV s<sup>-1</sup> scan rate; (b) variation of the area of the CV loops as a function of Fe<sub>3</sub>O<sub>4</sub> content, calculated from (a); (c) CV loops of the MoS<sub>2</sub>/(3%) Fe<sub>3</sub>O<sub>4</sub> nanocomposite at scan rates of 20 to 100 mV s<sup>-1</sup>; (d) Tafel's slope (fitted red line – MoS<sub>2</sub>/(3%) Fe<sub>3</sub>O<sub>4</sub>; fitted blue line – pure MoS<sub>2</sub>); variation in contribution ratio as a function of scan rates for (e) pure MoS<sub>2</sub> and (f) MoS<sub>2</sub>/(3%) Fe<sub>3</sub>O<sub>4</sub> nanocomposite.

of both faradaic and capacitive mechanisms, stipulating a mixed charge storage behavior involving both diffusion-controlled redox reactions and capacitive storage.<sup>70,71</sup> In note S3(A) (ESI†), detailed calculation of the Tafel slope is provided. The Tafel slopes for MoS<sub>2</sub> and MoS<sub>2</sub>/(3%) Fe<sub>3</sub>O<sub>4</sub> as shown in Fig. 7(d) were determined to be 0.57 and 0.60, respectively, both suggesting a charge storage mechanism that combines both the faradaic and the capacitive processes. A Tafel slope of 0.57 indicates a stronger influence of the faradaic process, implying that charge storage is more diffusion-controlled with a

capacitive component. Conversely, a Tafel slope of 0.60 indicates a higher capacitive contribution, reflecting a more balanced combination of faradaic and capacitive behaviors. Although both materials exhibit mixed charge storage mechanisms, the slightly higher value of the Tafel slope for MoS<sub>2</sub>/(3%) Fe<sub>3</sub>O<sub>4</sub> points toward an increased capacitive behavior compared to MoS<sub>2</sub> alone.

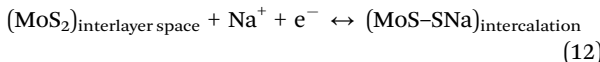
Now, pseudocapacitance may result from processes like underpotential deposition, intercalation, and surface redox reactions. The mechanism of underpotential deposition

involves the adsorption or desorption of alkali cations at the electrode/electrolyte interface through a surface process, such as

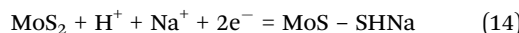
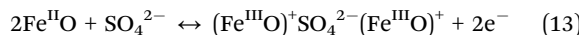


In the case of highly disordered materials, this underpotential deposition process has the most significant contribution. During underpotential deposition,  $\text{Na}^+$  ions get attracted to the surface of the  $\text{MoS}_2$  nanostructures from the electrolyte solution at a potential lower than the equilibrium value for the deposition to occur, as the presence of surface defects tends to suppress the deposition potential below its equilibrium value. This results in the formation of a thin layer of  $\text{Na}^+$  ions on the defect rich  $\text{MoS}_2$  surface. This dynamic interaction at the interface contributes to the overall charge storage mechanism by influencing the surface electrochemical behavior of the  $\text{MoS}_2$  nanostructures.<sup>72</sup>

The second mechanism, known as the intercalation process, involves the insertion of the alkali cations ( $\text{Na}^+$ ) into the layered structure of  $\text{MoS}_2$  from electrolyte and/or extraction of the alkali cations ( $\text{Na}^+$ ) from the layered structure of  $\text{MoS}_2$  to the electrolyte. In this structure, layers of molybdenum atoms are sandwiched between layers of sulfur atoms, forming its crystallographic framework. During charging, alkali  $\text{Na}^+$  ions penetrate into the space between the consecutive sandwich structures of  $\text{MoS}_2$  atomic layers from the electrolyte without causing any noticeable dimensional distortion of the overall crystal lattice. Conversely, during discharging, these ions are released back into the electrolyte. Thus, the intercalation and deintercalation processes are facilitated by the layered structure of  $\text{MoS}_2$ .<sup>73–76</sup> This reversible movement of ions enhances the charge storage capacity of the supercapacitor by utilizing the space within the layered structure. The intercalation process can be represented by the following equation:



The intercalation/de-intercalation process is favored by both the pristine  $\text{MoS}_2$  and the  $\text{MoS}_2/\text{Fe}_3\text{O}_4$  nanocomposites during the fast and reversible successive surface redox reactions. In the presence of magnetite, the  $\text{Fe}^{2+}$  ions can get oxidized to  $\text{Fe}^{3+}$  by donating electrons, and to balance this positive charge, sulfate ions from the electrolyte intercalate into the layered structure of  $\text{MoS}_2$ . Simultaneously,  $\text{Na}^+$  and  $\text{H}^+$  ions from the solution also intercalate in between the  $\text{MoS}_2$  layers to accept the donated electrons.<sup>77</sup> These processes result in the formation of conjugates, as shown in the following equations:



So, from the above discussions, it can readily be inferred that the presence of magnetite nanodiamonds not only enhances the ionic intercalation through the layered structure but also expedites the redox process following the intercalation.

Now, the equation given below can be used to investigate the reaction kinetics:

$$i = k_1v + k_2v^{1/2} \quad (15)$$

Here,  $k_1v$  represents the capacitive current and  $k_2v^{1/2}$  corresponds to the current from a diffusion-controlled process.  $k_1$  and  $k_2$  are constants, and  $v$  ( $\text{mV s}^{-1}$ ) is the scan rate. Now eqn (15) can be rearranged to a form as given below:

$$\frac{i}{v^{1/2}} = k_1v^{1/2} + k_2 \quad (16)$$

Now, using eqn (16), both  $k_1$  and  $k_2$  can be obtained from the slope and  $y$ -intercept of the  $i/v^{1/2}$  vs.  $v^{1/2}$  plot, respectively. In Supplementary note S3(B) (ESI†), the detailed analysis of current contribution is provided. Fig. 7(e and f) shows that as the scan rate increases, the capacitive contribution of the materials increases, while the diffusion contribution decreases.<sup>78,79</sup> This phenomenon arises from the fact that a significant decrease in the speed of potential sweep across the electrode at lower scan rates provides an ample amount of time for the diffusion of electrolyte ions or molecules to occur. However, when the scan rate is increased, the potential sweep becomes too fast for the ionic diffusion to occur, resulting in a reduction in diffusion contribution to current density. On the other hand, the double-layer capacitor undergoes charging and discharging due to the alternation of voltage in cyclic voltammetry measurements, resulting in a capacitive current response. When the scan rates are high ( $100 \text{ mV s}^{-1}$ ), a more noticeable contribution of capacitive current is observed, as at high scan rates the potential changes rapidly, requiring the electric double layer at the electrode/electrolyte interface to charge and discharge quickly. This leads to an enhancement in capacitive current arising from an escalated rate of electrode surface charge accumulation (charging) and deaccumulation (discharging) at elevated scan rates.<sup>80</sup>

Achieving an optimal balance between capacitive and diffusion contributions is vital for ensuring effective energy utilization, rapid energy distribution, stability and a prolonged lifespan for the energy storage devices. When capacitive processes are more significant than diffusion-controlled ones, the system's ability to store energy becomes restricted, leading to a diminution in overall energy density. If diffusion processes are too dominant, the supercapacitor may experience slow charge-discharge rates and struggles to meet high-power demands. Therefore, the  $\text{MoS}_2/(3\%) \text{Fe}_3\text{O}_4$  nanocomposite, as shown in Fig. 7(f), is more likely to achieve a better balance between capacitive and diffusion currents than pure  $\text{MoS}_2$  nanoflowers, leading to improved energy storage, higher energy and power densities, and overall better performance.

The CV responses of the  $\text{MoS}_2/(3\%) \text{Fe}_3\text{O}_4$  nanocomposite electrode in Fig. 7(c) exhibit a gradual transition towards a more spindle-shaped loop as the scan rate increases from 20 to  $100 \text{ mV s}^{-1}$ . At slow scan rates, the electrolyte ions have sufficient time to diffuse towards the electrode surface, allowing them to thoroughly penetrate the porous  $\text{MoS}_2$  nanoflowers and fully utilize the active surface sites within the nano-petal structure. This extensive interaction enables a large amount of charge



to be stored, thereby increasing the material's specific capacitance. On the other hand, at faster scan rates, the time available for the electrolyte ions to reach the inner nanoporous surface of the  $\text{MoS}_2$  nanoflowers becomes limited. Consequently, the ions are limited to interacting solely with the active sites that are easily reachable on the outer surface. Hence the inner structure is not fully utilized for storing charges, culminating in a decrement in overall capacitance.<sup>81</sup> Furthermore, at high scan rates, the electrode potential undergoes rapid alteration, causing the potential to shift suddenly, and hence the electrode faces difficulties in achieving equilibrium, which leads to polarization. This polarization effect hinders the charge transfer between the surface of the electrode material and the electrolyte, causing the capacitance to fall.<sup>82-84</sup>

### Galvanostatic charge-discharge (GCD)

Among all electrochemical measurements, galvanostatic charging-discharging (GCD) can be used directly to determine the charge storage capacity of a material. The GCD technique more closely mimics the real-world applications and provides more accurate quantitative information compared to the CV measurement of any material. Fig. 8(a) shows the GCD curves of all samples at a current density of  $0.3 \text{ A g}^{-1}$  within a potential window of  $-0.2$  to  $0.4$  V. A pseudocapacitive charge storage mechanism can be identified by the deviation of the GCD curve from the usual symmetrical triangular-shape. According to eqn (12)–(14), the intercalation of  $\text{Na}^+$  ions from the electrolyte into the space between the atomic layers of the crystal structure may lead to pseudocapacitive behavior.<sup>30</sup>

Fig. 8(b) depicts the GCD curves of the  $\text{MoS}_2/(3\%) \text{Fe}_3\text{O}_4$  nanocomposite at different current densities. The specific capacitance of the nanocomposite, as determined from the GCD curves, decreases as the current density increases (as shown in the inset of Fig. 8(b)). The observed pattern of decreasing specific capacitance at higher current densities is a common phenomenon. At very low current densities, ions in the electrolyte have sufficient time to diffuse and reach all the active sites of the

electrode, allowing for the complete insertion and extraction of ions within the electrode material. This allows the electrode to utilize its full capacity to store charge, leading to a higher specific capacitance.<sup>85</sup> Conversely, at higher current densities, the limited time available for ionic diffusion prevents ions from effectively reaching all the active sites of the electrode interior, permitting only the outer surface regions of the electrode to contribute to the capacitance, rather than the bulk of the material. This restricted ionic movement and incomplete utilization of the electrode's active sites lead to a reduction in specific capacitance.<sup>86</sup>

Fig. 9 illustrates the changes in specific capacitance and discharge time of nanostructured  $\text{MoS}_2$  and  $\text{MoS}_2/\text{Fe}_3\text{O}_4$  composites obtained from the GCD measurements (Fig. 8(a)) at a current density of  $0.30 \text{ A g}^{-1}$ . The specific capacitance ( $C_{sp}$ ) was determined by applying the following equation:

$$C_{sp} = \frac{I \times \Delta t}{m \times \Delta V} \quad (17)$$

where  $m$  is the mass of active materials (g),  $\Delta t$  the discharge time (s),  $I$  the discharge current (A), and  $\Delta V$  the potential window (V). Fig. 9(a) shows that the specific capacitance of  $\text{MoS}_2$  nanoflowers with up to  $3\%$   $\text{Fe}_3\text{O}_4$  nanodiamond incorporation increases to a value of  $712 \text{ F g}^{-1}$ , which is approximately three times higher than that of the pure  $\text{MoS}_2$  nanoflower. However, beyond this weight percentage, the specific capacitance drops by  $\sim 50\%$ . On the other hand, Fig. 9(b) shows that the  $\text{MoS}_2/(3\%) \text{Fe}_3\text{O}_4$  nanocomposite also exhibits the longest discharge time of 1423 seconds, compared to 517 seconds for pure  $\text{MoS}_2$ , 890 seconds for  $\text{MoS}_2/(1\%) \text{Fe}_3\text{O}_4$ , and 730 seconds for  $\text{MoS}_2/(5\%) \text{Fe}_3\text{O}_4$ . This extended discharge time suggests that the  $\text{MoS}_2/(3\%) \text{Fe}_3\text{O}_4$  nanocomposite supports the most effective  $\text{Na}^+$  ion insertion into the nanostructure. The highest specific capacitance of the  $\text{MoS}_2/(3\%) \text{Fe}_3\text{O}_4$  composite can be attributed to its smaller crystallite size, increased dislocation density and disorder, which is evident from the gradual increase in the stacking faults in  $\text{MoS}_2$  as the  $\text{Fe}_3\text{O}_4$  content increases up to  $3\%$ , as

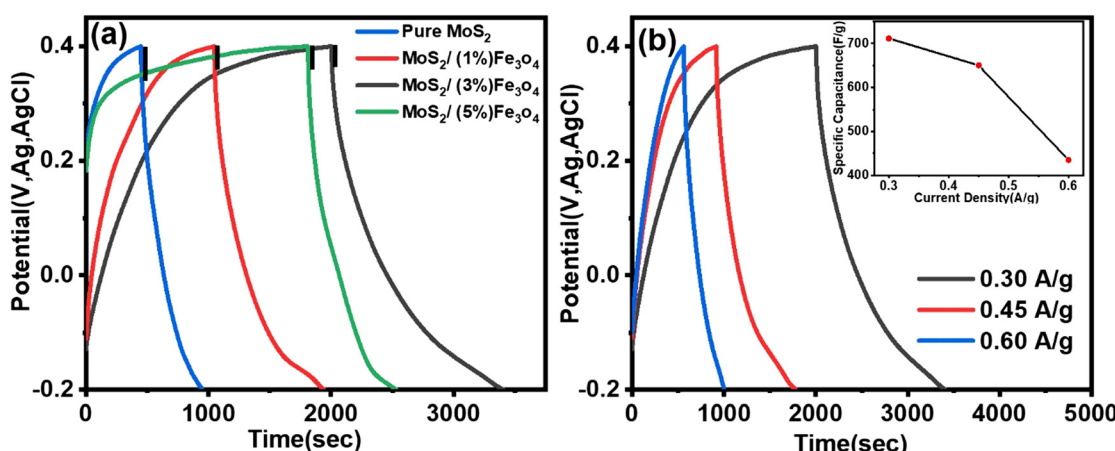


Fig. 8 (a) GCD curves of  $\text{MoS}_2$  nanoflowers and  $\text{MoS}_2/\text{Fe}_3\text{O}_4$  nanocomposites at a specific current density of  $0.30 \text{ A g}^{-1}$  (IR-drop of all electrode materials is indicated by black vertical lines); (b) GCD curves of the  $\text{MoS}_2/(3\%) \text{Fe}_3\text{O}_4$  nanocomposite at different current densities (the inset shows the specific capacitance variation of the  $\text{MoS}_2/(3\%) \text{Fe}_3\text{O}_4$  nanocomposite as a function of current density).



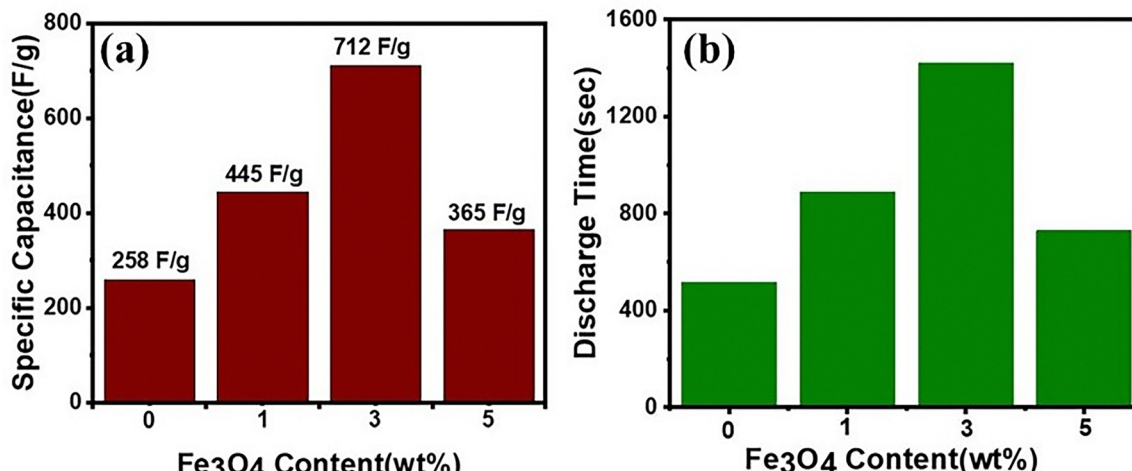


Fig. 9 (a) Specific capacitance of the samples versus  $\text{Fe}_3\text{O}_4$  content, with the  $\text{MoS}_2$ /(3%)  $\text{Fe}_3\text{O}_4$  nanocomposite exhibiting the highest specific capacitance; (b) discharge time of the samples relative to  $\text{Fe}_3\text{O}_4$  content, as determined from the GCD curves shown in Fig. 8(a).

illustrated in Fig. 4. The increased structural distortion, leading to numerous defects and disordered regions, could in turn enhance the effective surface area and redox reaction sites. Apart from that the gradual expansion of lattice spacing in  $\text{MoS}_2$ / $\text{Fe}_3\text{O}_4$  nanocomposites with up to 3%  $\text{Fe}_3\text{O}_4$  incorporation as shown in Fig. 6(f) improves the material's charge storage capabilities by generating more space between the parallel atomic planes, facilitating an efficient  $\text{Na}^+$  ion intercalation within the electrode. Additionally, the increase in effective surface area due to the enhanced surface-defect induced disorder improves the material's electric double-layer capacitance (EDLC), associated with the storage of charge at the interface between the electrode and the electrolyte. This increased effective surface area facilitates more efficient ion adsorption and desorption processes, thereby enhancing the overall energy storage capacity of the device.<sup>87-89</sup>

Nevertheless, the crystallite size increased significantly when the  $\text{Fe}_3\text{O}_4$  content exceeded 3%, leading to a decline in capacitive performance during GCD measurements, as depicted in Fig. 9(a), compared to the  $\text{MoS}_2$ /(3%)  $\text{Fe}_3\text{O}_4$  nanocomposite. Moreover, the collapsed nanoporous electrolytic channels in  $\text{MoS}_2$ /(5%)  $\text{Fe}_3\text{O}_4$  by the protruding  $\text{Fe}_3\text{O}_4$  nanodiamonds as described previously could contribute significantly towards the observed reduction in specific capacitance by blocking effective percolation of the electrolyte into the bulk and thus diminishing the effective electrode/electrolyte contact area or available active electrode surface sites.

Additionally, in Fig. 8(a), a rapid drop in potential can be observed at the beginning of the discharging phase, indicating energy dissipation caused by internal resistance.<sup>90</sup> The  $\text{MoS}_2$ / $\text{Fe}_3\text{O}_4$  nanocomposite electrodes exhibit relatively small abrupt potential drop (IR drop) compared to the pure  $\text{MoS}_2$  electrode, indirectly suggesting that the incorporation of  $\text{Fe}_3\text{O}_4$  into  $\text{MoS}_2$  nanoflowers results in higher conductivity or reduced internal resistance. The decrease in internal resistance could be partly attributed to the development of structural imperfections (vacancies and interstitials), the presence of  $\text{Fe}_3\text{O}_4$  with

multiple oxidation states and narrow conducting pathways generated by the possible cation exchange across the  $\text{MoS}_2$ – $\text{Fe}_3\text{O}_4$  interface, as discussed before. The enhanced conductivity could improve charge transportation dynamics within the system. It has also been suggested that incorporation of  $\text{Fe}_3\text{O}_4$  nanodiamonds into pure  $\text{MoS}_2$  decreases the self-discharging phenomenon, leading to a minimal voltage drop and an increase in discharge time.<sup>91</sup>

#### Electrochemical impedance spectroscopy (EIS)

Electrochemical impedance spectroscopic (EIS) analysis can provide additional evidence to support the influence of conductivity and internal resistance on the specific capacitance trend of nanocomposites. The EIS measurements were conducted to assess the resistive characteristics and gain insights into the charge transfer mechanisms of both pure  $\text{MoS}_2$  and composite electrodes. The fitted Nyquist plots for all samples are shown in Fig. 10, highlighting different regions that correspond to charge transfer-limited and diffusion-limited processes in the supercapacitor. Conventionally, a high-frequency semicircle and a low-frequency inclined line can be differentiated by the knee frequency, as shown in Fig. 10.

In the high frequency region, the intersection of the semicircle with the real impedance axis with a non-zero value represents the equivalent series resistance ( $R_s$ ) which is a combination of the interfacial resistance between the electrode and the current collector, the intrinsic ionic electrolyte resistance, and the internal resistance of the electroactive materials.<sup>92</sup> In the high-to-medium frequency range, the semicircle corresponds to a parallel combination of the constant phase element (CPE) and the charge transfer resistance ( $R_{ct}$ ). The CPE signifies the non-ideal capacitive behavior of the electrochemical system. In the low frequency region, the straight line, inclined to the  $Z'$ -axis of the Nyquist plot, represents the Warburg impedance ( $Z_w$ ), which describes the impedance associated with the ionic diffusion in the electrolyte. An equivalent Randle's circuit, as shown in the insets of Fig. 10,



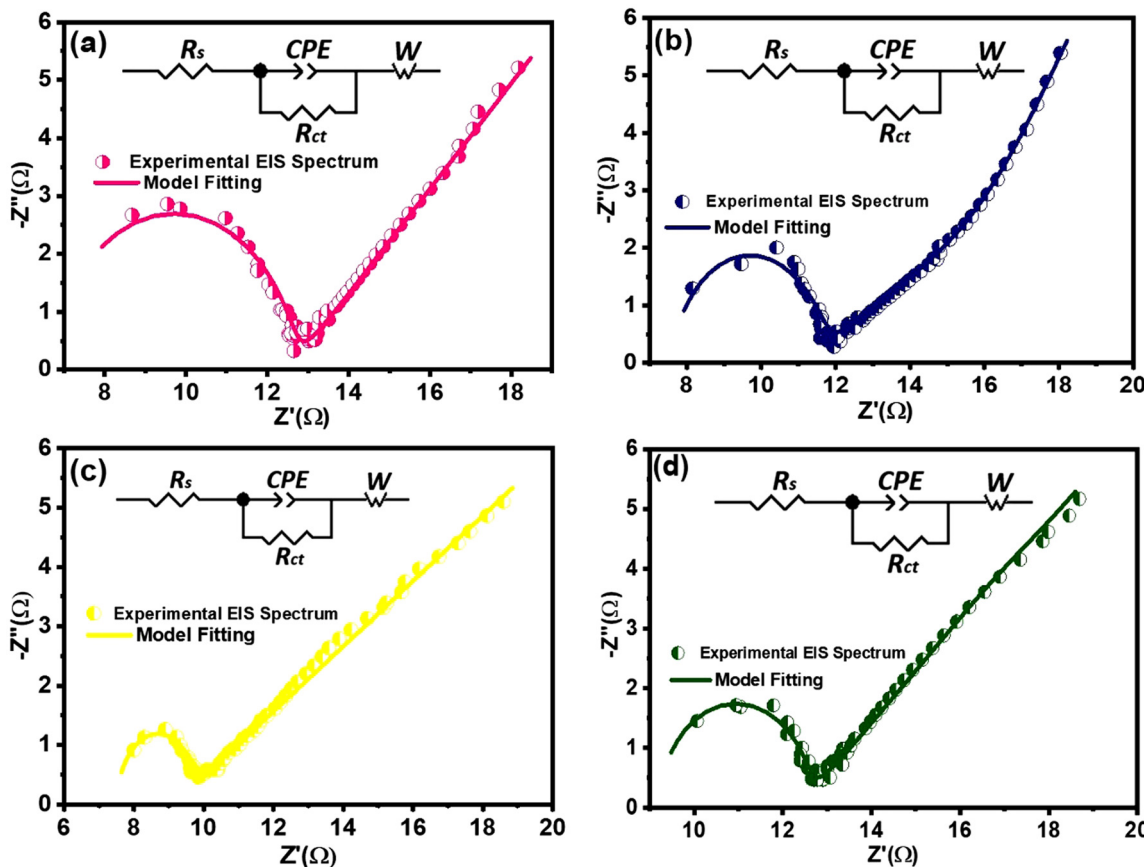


Fig. 10 EIS spectra of (a) pure  $\text{MoS}_2$  nanoflowers; (b)  $\text{MoS}_2/(1\%) \text{Fe}_3\text{O}_4$  nanocomposite; (c)  $\text{MoS}_2/(3\%) \text{Fe}_3\text{O}_4$  nanocomposite; and (d)  $\text{MoS}_2/(5\%) \text{Fe}_3\text{O}_4$  nanocomposite electrodes. The solid lines indicate the fitted data. The inset of all graphs shows equivalent Randle's circuit with which the experimental EIS data were fitted to extract the values of different electrical components of the circuit.

was adopted to simulate the experimental EIS spectra using *Z* View software, to extract various electrical components of the circuit.

According to the fitting circuit, the  $\text{MoS}_2/(3\%) \text{Fe}_3\text{O}_4$  composite exhibits a rather low  $R_s$  value among all the nanocomposites as shown in Table 1. This could be attributed to the optimum incorporation of  $\text{Fe}_3\text{O}_4$  nanodiamonds. However, in the case of magnetite, above the Verwey transition temperature ( $>120$  K), the density of states at the Fermi level is non-zero, and it conducts electricity effectively behaving like a zero-band-gap material.<sup>93</sup> Thus,  $\text{Fe}_3\text{O}_4$  behaves like a metal at room temperature, where conductivity arises from electron hopping between  $\text{Fe}^{2+}$  and  $\text{Fe}^{3+}$  ions in its inverse spinel structure.<sup>94</sup> Now, depending on the extent of interdiffusion of ions across the solid interface, two common scenarios may arise. On the

one hand, the work function of the  $\text{Fe}_3\text{O}_4$  phase could be considerably greater than that of  $\text{MoS}_2$ , and on the other hand, the work function of the  $\text{Fe}_3\text{O}_4$  phase could be smaller than or very close to that of  $\text{MoS}_2$ , if not smaller. Now, in the case of predominant migration of  $\text{Fe}^{2+}/\text{Fe}^{3+}$  ions across the interface to the  $\text{MoS}_2$  phase, some extra free carriers are expected to be generated within the  $\text{MoS}_2$  lattice causing the Fermi level of  $\text{MoS}_2$  to rise above that of  $\text{Fe}_3\text{O}_4$ . In such case, the chemical equilibrium is attained through migration of free carriers across the interface to level-off the Fermi energy levels of the two phases in contact, and consequently, a Schottky-type interface potential barrier could form at the  $\text{Fe}_3\text{O}_4$ – $\text{MoS}_2$  interface. On the other hand, in the case of predominant migration of  $\text{Mo}^{4+}$  ions into the  $\text{Fe}_3\text{O}_4$  lattice, some extra free carriers are expected to be generated within the magnetite lattice causing its Fermi level to rise above that of  $\text{MoS}_2$ . In such case, to establish chemical equilibrium, the Fermi levels of both phases are levelled off through transfer of electrons from  $\text{Fe}_3\text{O}_4$  to  $\text{MoS}_2$  near the interface region causing the band to bend in such a way that pure ohmic contact is generated between the two phases. Now, following the EIS study of the nanocomposite system as depicted in Fig. 10, it can be reasonably inferred that no strong Schottky type potential barrier could have formed at the  $\text{Fe}_3\text{O}_4$ – $\text{MoS}_2$  interface, as no prominent feature other than a

Table 1 Fitted values of Randle's circuit elements for pure  $\text{MoS}_2$  and  $\text{MoS}_2/\text{Fe}_3\text{O}_4$  nanocomposites

Electrode	$R_s$ ( $\Omega$ )	$R_{ct}$ ( $\Omega$ )	$Z_w$ ( $\Omega$ )
Pure $\text{MoS}_2$	6.7	5.9	18.09
$\text{MoS}_2/(1\%) \text{Fe}_3\text{O}_4$	9.2	3.2	23.79
$\text{MoS}_2/(3\%) \text{Fe}_3\text{O}_4$	7.3	1.8	11.56
$\text{MoS}_2/(5\%) \text{Fe}_3\text{O}_4$	7.5	3.83	11.93

single semicircle, a linear inclined slope and a high frequency intercept at the real axis of the Nyquist plot obtained from the extrapolation of the semicircle, consecutively associated with the electrode–electrolyte interfacial charge transfer process, Warburg diffusion and the internal resistance, could be observed in support of an interface potential barrier. However, the formation of a pure resistive contact at the interface can readily be justified by considering it as a contributor towards the overall series resistive component  $R_s$  in the EIS spectra. Nonetheless, it is not unlikely that a weak Schottky potential could have formed at the interface, the effect of which is approximately similar to that of the resistive effect. Therefore, the presence of dispersed  $\text{Fe}_3\text{O}_4$  nanodiamonds in  $\text{MoS}_2$  nanoflowers act like localized regions of conductive sinks, which could effectively reduce the equivalent series resistance ( $R_s$ ), as observed from the EIS data in Table 1, particularly for the  $\text{MoS}_2$ /(3%)  $\text{Fe}_3\text{O}_4$  sample. The lower  $R_s$  indicates minimal energy loss during electron flow through the bulk of the material system, indirectly indicating an improved bulk electrode material conductivity under the assumption that the electrode–collector contact resistance remains unchanged. Such enhanced bulk electrode conductivity not only facilitates faster electron transfer but also supports improved discharging behavior through reduction in linear potential drop as indicated by the reduced IR loss in the GCD response of  $\text{MoS}_2/\text{Fe}_3\text{O}_4$  nanocomposites compared to pure  $\text{MoS}_2$  nanoflowers (Fig. 8(a)).<sup>95</sup>

The diameter of the semicircle of the Nyquist plot is directly related to the charge transfer resistance ( $R_{ct}$ ) at the interface between the electrode and the electrolyte. The  $\text{MoS}_2$ /(3%)  $\text{Fe}_3\text{O}_4$  nanocomposite exhibits the smallest semicircle diameter, signifying the lowest  $R_{ct}$  (1.8  $\Omega$ ) compared to both pristine and other nanocomposite samples as shown in Table 1. It has already been argued that introducing diamond-shaped  $\text{Fe}_3\text{O}_4$  nanoparticles into  $\text{MoS}_2$  nanoflowers can create a synergistic effect by enhancing the specific surface area, defect induced active surface sites and lattice interlayer spacing of the nanocomposites which in turn can promote charge transfer across the interface between the electrode and the electrolyte, causing the nanocomposite to surpass pure  $\text{MoS}_2$  in terms of electrochemical performance.<sup>96</sup> The lowest  $R_{ct}$  value of the  $\text{MoS}_2$ /(3%)  $\text{Fe}_3\text{O}_4$  nanocomposite suggests that 3%  $\text{Fe}_3\text{O}_4$  content is optimal for improving the charge transportation across the electrode/electrolyte interface. However, increasing the  $\text{Fe}_3\text{O}_4$  content beyond this level causes random fragmentation of the  $\text{MoS}_2$  nanopetals which accumulate in the form of discarded piles of detached petals partly blocking the nanoporous channels and hence the active surface sites deeper inside the nanoflowers for redox reaction to occur, as discussed in the previous sections. These blockages could also hamper the  $\text{Na}^+$  intercalation process and lead to an increase in charge transfer resistance.

In the Nyquist plot, all the 3-electrode systems display a slope between 45° and 90° in the low-frequency range, indicating a combination of capacitive and diffusion-controlled behaviors.<sup>77</sup> From Table 1, it is evident that the  $\text{MoS}_2$ /(3%)  $\text{Fe}_3\text{O}_4$  3-electrode system has the lowest Warburg impedance

( $Z_w$ ) of 11.56  $\Omega$  compared to the other systems, suggesting that the given system has a superior ionic diffusion transportation capability than others. This observation indirectly suggests that an efficient ionic intercalation through the broadened crystallographic interlayer spacing of the  $\text{MoS}_2$ /(3%)  $\text{Fe}_3\text{O}_4$  composite renders a steeper ionic gradient in the electrolyte, by effectively limiting any type of ionic charge accumulation at the electrode–electrolyte interface. This in turn allows for an enhanced ionic diffusion drive through the electrolyte and thus lowers the Warburg impedance to some extent that contributes towards the improved specific capacitance of the sample. Hence, the EIS result is also consistent with the CV and GCD analyses, demonstrating that the nanostructured composites have lower resistance for charge migration between the electrolyte and the electrode compared to pristine  $\text{MoS}_2$  nanoflowers.

### Cyclic stability

Long-term cyclic stability is crucial for any supercapacitor based device. The  $\text{MoS}_2$ /(3%)  $\text{Fe}_3\text{O}_4$  nanocomposite demonstrated the highest specific capacitance compared to all other samples in this study. Thus, it was subjected to repeated GCD measurements to evaluate its capacitance retention capability and coulombic efficiency over 10 000 cycles, as depicted in Fig. 11. The calculations of capacitance retention and coulombic efficiency were performed using the following equations:

$$\text{Capacitance retention (\%)} = \frac{\text{nth cycle capacitance}}{\text{1st cycle capacitance}} \times 100 \quad (18)$$

$$\text{Coulombic efficiency, } \eta = \frac{t_{\text{discharge}}}{t_{\text{charge}}} \times 100 \quad (19)$$

In eqn (19),  $t_{\text{discharge}}$  refers to the time duration the system requires to release its stored energy or discharge, while  $t_{\text{charge}}$  represents the time needed to fully charge the system. As shown in Fig. 11, the  $\text{MoS}_2$ /(3%)  $\text{Fe}_3\text{O}_4$  nanocomposite electrode retained 84% of its initial specific capacitance after 10 000 charge–discharge cyclic loading at a current density of 2 A g<sup>-1</sup>, demonstrating good cyclic stability. Fig. 11 also shows that after 5000 cycles, the coulombic efficiency is ~94%, which rises to 103% after 10 000 cycles. This level of retention at the given current density suggests that the system preserves a significant portion of its energy storage capacity even after extensive cycling, which is a rather desirable feature for practical applications. However, a monotonic reduction in capacitance retention is observed in Fig. 11. As the system undergoes repeated charging–discharging cycles, the mechanical stress associated with repeated cycling can lead to the collapse of the electrode structure and separation of active materials from the electrode. Such deterioration in structural integrity reduces the effective contact area between the active material and the electrolyte, which is essential for efficient interfacial charge transfer and energy storage. As the contact area decreases, the capacitance of the system decreases, resulting in a decrease in performance. The materials' detachment not only reduces the effective area for charge transfer but also results in the dissolution of active



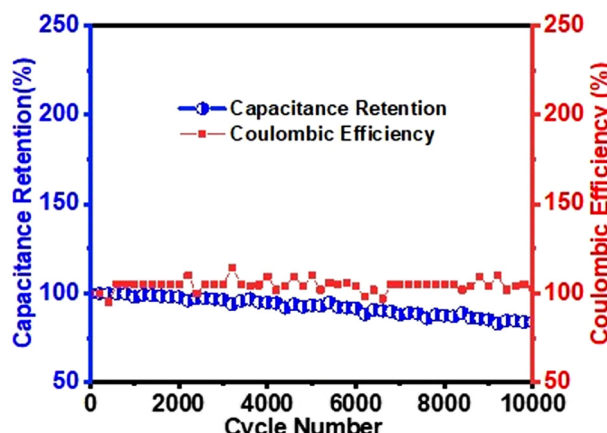


Fig. 11 Long-term cyclic stability performance showing capacitance retention and coulombic efficiency of the  $\text{MoS}_2$ /(3%)  $\text{Fe}_3\text{O}_4$  nanocomposite sample measured at a current density of  $2 \text{ A g}^{-1}$  over 10 000 cycles.

materials into the electrolyte and alters its ionic transportation property. Nonetheless, as the contact between the electrode and the current collector weakens due to electrode disintegration, the system becomes less efficient at storing and releasing charge, leading to a drop in specific capacitance.<sup>34,97</sup>

The efficiency value obtained from eqn (19), expressed as percentage, reflects how effectively the system utilizes the charge collected during the charging process. A higher coulombic efficiency indicates better performance, as more of the input energy is retained and made available during the discharging phase. Fig. 11 shows that after 4000 cycles, the coulombic efficiency is  $\sim 95\%$ , which rises to  $103\%$  after 10 000 cycles, highlighting the exceptional stability of the  $\text{MoS}_2$ /(3%)  $\text{Fe}_3\text{O}_4$  composite. Here, the electrode's exceptional cycling stability and high efficiency can be attributed to its long-lasting structural integrity and improved ionic diffusion within the pores over time.<sup>98,99</sup> Overall, the nanocomposite's advantageous morphological and structural features contribute to its stability, as evidenced by the analyses.

The comparative analysis of  $\text{MoS}_2/\text{Fe}_3\text{O}_4$  based composites reveals the superior performance in the current study, which employs a hydrothermal synthesis route to create defect-rich  $\text{MoS}_2$  nanoflowers with 3% diamond-shaped  $\text{Fe}_3\text{O}_4$  nanoparticles as shown in Table ST1. This work achieves a specific capacitance of  $712 \text{ F g}^{-1}$  at  $0.3 \text{ A g}^{-1}$ , which outperforms the 2D  $\text{MoS}_2$  sheets with polygonal-shaped  $\text{Fe}_3\text{O}_4$ , the flower-like  $\text{MoS}_2$  with spherical  $\text{Fe}_3\text{O}_4$ , the sheet-like  $\text{MoS}_2$  with nonuniform spherical  $\text{Fe}_3\text{O}_4$  and the  $\text{MoS}_2$  nanosheets with uniform sized  $\text{Fe}_3\text{O}_4$  nanoparticles exhibiting specific capacitances of  $401 \text{ F g}^{-1}$  (at  $0.5 \text{ A g}^{-1}$ ),<sup>33</sup>  $522.7 \text{ F g}^{-1}$  (at  $0.5 \text{ A g}^{-1}$ ),<sup>35</sup>  $527 \text{ F g}^{-1}$  (at  $0.5 \text{ mA cm}^{-2}$ )<sup>34</sup> and  $670 \text{ F g}^{-1}$  (at  $0.25 \text{ A g}^{-1}$ ),<sup>36</sup> respectively. In terms of capacitance retention, our optimized material also outperforms by retaining  $94\%$  after 5000 cycles ( $84\%$  after 10 000 cycles), compared to  $89.3\%$  after 5000 cycles for the  $\text{Fe}_3\text{O}_4/\text{MoS}_2/\text{PANI}$  composite synthesized by a hydrothermal method and  $76\%$  after 2000 cycles for the  $\text{MoS}_2/\text{Fe}_3\text{O}_4$  composite synthesized *via* thermal decomposition. The distinctive defect-rich nanoflower morphology combined with  $\text{Fe}_3\text{O}_4$  nanodiamonds provides numerous active sites, as discussed previously. This contributes to the exceptional electrochemical properties observed in the current study, establishing it as one of the most promising candidates among the most recently developed  $\text{MoS}_2/\text{Fe}_3\text{O}_4$  based nanostructured composites in terms of both specific capacitance and long-term stability.

To investigate the reduction of capacitance retention, EIS measurements were performed before and after the cycling test. Fig. 12 shows the Nyquist plots for  $\text{MoS}_2$ /(3%)  $\text{Fe}_3\text{O}_4$  before and after the cycling test. The extracted data from the fittings (using ZView software) shown in Table ST2 (ESI†) reveal that  $R_s$ ,  $R_{ct}$  and  $Z_w$  increased by  $8.2\%$ ,  $27.8\%$  and  $1.3\%$ , respectively, following the long-term GCD cyclic loading process. Here the noticeable rise in  $R_{ct}$  suggests a reduced efficiency of interfacial charge transfer due to structural degradation. Over an extended cyclic loading, however, the mechanical damage of the network of microstructural channels limits the availability of active redox sites by restricting the specific surface area of the interfaces, causes loss of disintegrated active electrode material and

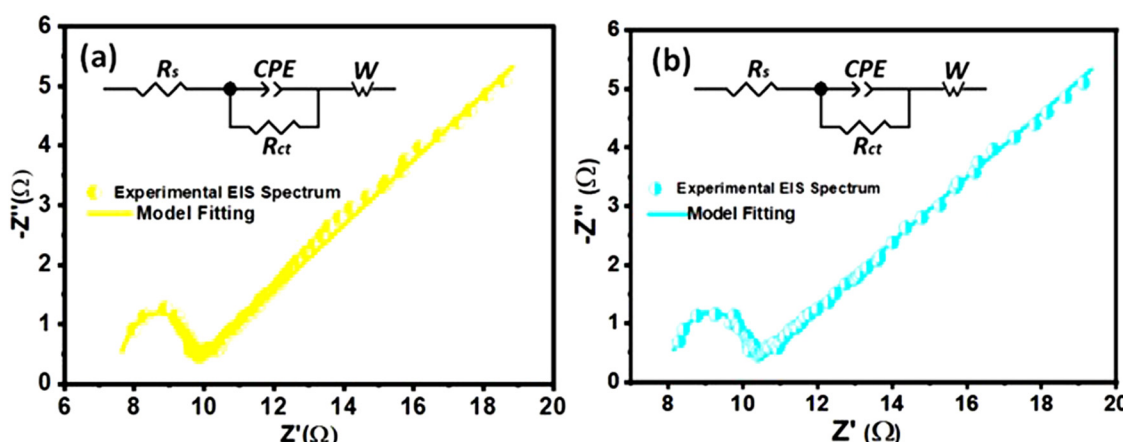


Fig. 12 EIS spectra of  $\text{MoS}_2$ /(3%)  $\text{Fe}_3\text{O}_4$  (a) before and (b) after the cyclic stability test. The solid lines indicate the fitted data. The inset of all graphs shows equivalent Randle's circuit with which the experimental EIS data were fitted to extract the values of different electrical components of the circuit.



Table 2 Comparison of specific capacitance and capacitance retention of the recently reported  $\text{MoS}_2$  and  $\text{MnO}_2$  based supercapacitor electrodes

Electrode	Synthesis route	Electrolyte	Specific capacitance ( $\text{F g}^{-1}$ )	Capacitance retention	Ref.
$\text{Fe}_3\text{O}_4/\text{MnO}_2/\text{RGOs}$	Hydrothermal	1 M $\text{Na}_2\text{SO}_4$	77.5 $\text{F g}^{-1}$ at 0.5 $\text{A g}^{-1}$	—	100
$\text{CNTs}/\text{MoS}_2/\text{Fe}_3\text{O}_4$	Hydrothermal	6 M KOH	522.7 $\text{F g}^{-1}$ at 0.5 $\text{A g}^{-1}$	—	35
$\text{Fe}_3\text{O}_4/\text{MoS}_2/\text{PANI}$	Hydrothermal	3 M KOH	401 $\text{F g}^{-1}$ at 0.5 $\text{A g}^{-1}$	91% after 4000 cycles	33
$\text{MoS}_2/\text{MnS}$	Hydrothermal	0.5 M $\text{Na}_2\text{SO}_4$	351 $\text{F g}^{-1}$ at 0.3 $\text{A g}^{-1}$	78% after 4000 cycles	32
rGO/CNT/ $\text{MnO}_2$	Hydrothermal	1 M $\text{Na}_2\text{SO}_4$	319 $\text{F g}^{-1}$ at 0.5 $\text{A g}^{-1}$	89% after 3000 cycles	101
$\text{MnO}_2$ nanospheres/carbon nanoparticles/graphene	Freeze-drying	1 M $\text{Na}_2\text{SO}_4$	255 $\text{F g}^{-1}$ at 0.5 $\text{A g}^{-1}$	83% after 1000 cycles	102
$\text{MnO}_2/\text{PPy}/\text{rGO}$	Sonication-induced assembly of aqueous dispersions	0.5 M $\text{Na}_2\text{SO}_4$	404 $\text{F g}^{-1}$ at 0.25 $\text{A g}^{-1}$	92% after 4000 cycles	103
$\text{MnO}_2/(3\%) \text{Fe}_3\text{O}_4$	Hydrothermal	0.5 M $\text{Na}_2\text{SO}_4$	459 $\text{F g}^{-1}$ at 0.3 $\text{A g}^{-1}$	75% after 4000 cycles	49
$\text{MoS}_2/\text{MnO}_2$	Hydrothermal	0.5 M $\text{Na}_2\text{SO}_4$	199.12 $\text{F g}^{-1}$ at 0.04 $\text{A g}^{-1}$	95% after 4000 cycles	31
$\text{MoS}_2/(3\%) \text{Fe}_3\text{O}_4$	Hydrothermal	0.5 M $\text{Na}_2\text{SO}_4$	712 $\text{F g}^{-1}$ at 0.3 $\text{A g}^{-1}$	95% after 4000 cycles; 84% after 10 000 cycles	This work

hampers ionic diffusion, thereby enhancing the resistive contributions from all three electrical components, with a conspicuous increment in electrode–electrolyte charge transfer resistance. This increase in post-cycling  $R_{\text{ct}}$  hinders faradaic activity by slackening the interfacial electron transfer kinetics.

Additionally, Table 2 presents some recently reported electrochemical data for various  $\text{MoS}_2$  and  $\text{MnO}_2$ -based electrodes with different structural and morphological characteristics. Here, our  $\text{MoS}_2/(3\%) \text{Fe}_3\text{O}_4$  shows the highest specific capacitance and % capacity retention among the reported nanocomposites. The superior capacitive performance clearly indicates that the hydrothermally prepared  $\text{MoS}_2/(3\%) \text{Fe}_3\text{O}_4$  nanocomposite is a very suitable candidate material for high-performance supercapacitor electrodes.<sup>100,101</sup>

## Two electrode system

Two-electrode systems are preferred over three-electrode systems in practical device applications. Therefore, a prototype supercapacitor was made using the optimized  $\text{MoS}_2/(3\%) \text{Fe}_3\text{O}_4$  nanocomposite as the electrode material, to evaluate its performance for real-world applications under symmetrical two-electrode configuration. In this setup, the  $\text{MoS}_2/(3\%) \text{Fe}_3\text{O}_4$  nanocomposite served as both the anode and cathode material. The electrolyte was 0.5 M  $\text{Na}_2\text{SO}_4$  solution. The Whatman filter paper acted as a separator, preventing direct contact between the two electrodes, and the electrolyte ensured ionic connectivity between them. Fig. 13 depicts the schematic diagram of the charge storage mechanism in a symmetric two-electrode system, where the charge storage process combines electric double-layer capacitance (EDLC) and pseudocapacitance. The pseudocapacitance contribution may arise from intercalation, underpotential deposition, and surface redox reactions, during charging, whereas these processes are reversed during discharging.

When an external voltage is applied to charge the electrodes,  $\text{Na}^+$  and  $\text{SO}_4^{2-}$  ions of the electrolyte solution move towards the respective electrode surfaces. The positive ions ( $\text{Na}^+$ ) migrate towards the negative electrode (cathode) and negative ions ( $\text{SO}_4^{2-}$ ) migrate towards the positive electrode (anode). Some of these ions get adsorbed onto the electrode surfaces, forming a layer called the inner Helmholtz plane (IHP). The adsorption of electrolyte ions on the surface is significantly influenced by the

presence of surface vacancies, as suggested by eqn (1) and (5). The cationic vacancies ( $\text{V}'''_{\text{Mo}}$ ) at the surface of the electrode function as negatively charged sites that attract positively charged  $\text{Na}^+$  ions, effectively stabilizing the double layer, as follows:



on the other hand, the anionic vacancies ( $\text{V}_S^{2\bullet}$ ) at the surface of the anode act as positively charged sites interacting with  $\text{SO}_4^{2-}$  ions, facilitating the formation of a double layer as follows:



The IHP is marked by high density of ions resulting from strong electrostatic interactions between the electrode surface and various charged species in the electrolyte. This region consists of highly ordered solvent molecules and ions due to higher electrostatic force, which are crucial for forming the electric double layer (EDL) and facilitating reversible redox reactions. The outer Helmholtz plane (OHP) lies beyond the IHP, which consists of ions that are less tightly bound to the electrode surface compared to those in the IHP. This layer serves as a transitional region between the bulk electrolyte and the IHP. Ions adsorbed in the IHP are closely bound, leading to charge separation physically, creating an area of high capacitance. The IHP and OHP together form the electric double layer (EDL), which stores higher energy near the electrode surface region. The diffuse layer, extending from the OHP to the bulk electrolyte, contains more mobile ions that are less influenced by the electrode surface. The diffuse layer, although not directly contributing to energy storage processes, plays a vital role in creating and maintaining the necessary conditions for pseudocapacitance or EDLC.

Fig. 13 shows that electrolyte ions can intercalate between the crystallographic layers of the  $\text{MoS}_2/(3\%) \text{Fe}_3\text{O}_4$  nanocomposite, which is known as ion intercalation. Defects such as vacancies increase the number of active sites available for intercalation. The defect sites can strongly interact with incoming ions, facilitating their adsorption and subsequent intercalation. Sulfur and molybdenum vacancies (according to eqn (1) and (5)) can enhance electrolyte ion intercalation by providing additional entry points and diffusion routes within the material's layered structure. The subsequent electrode REDOX reactions can be expressed as

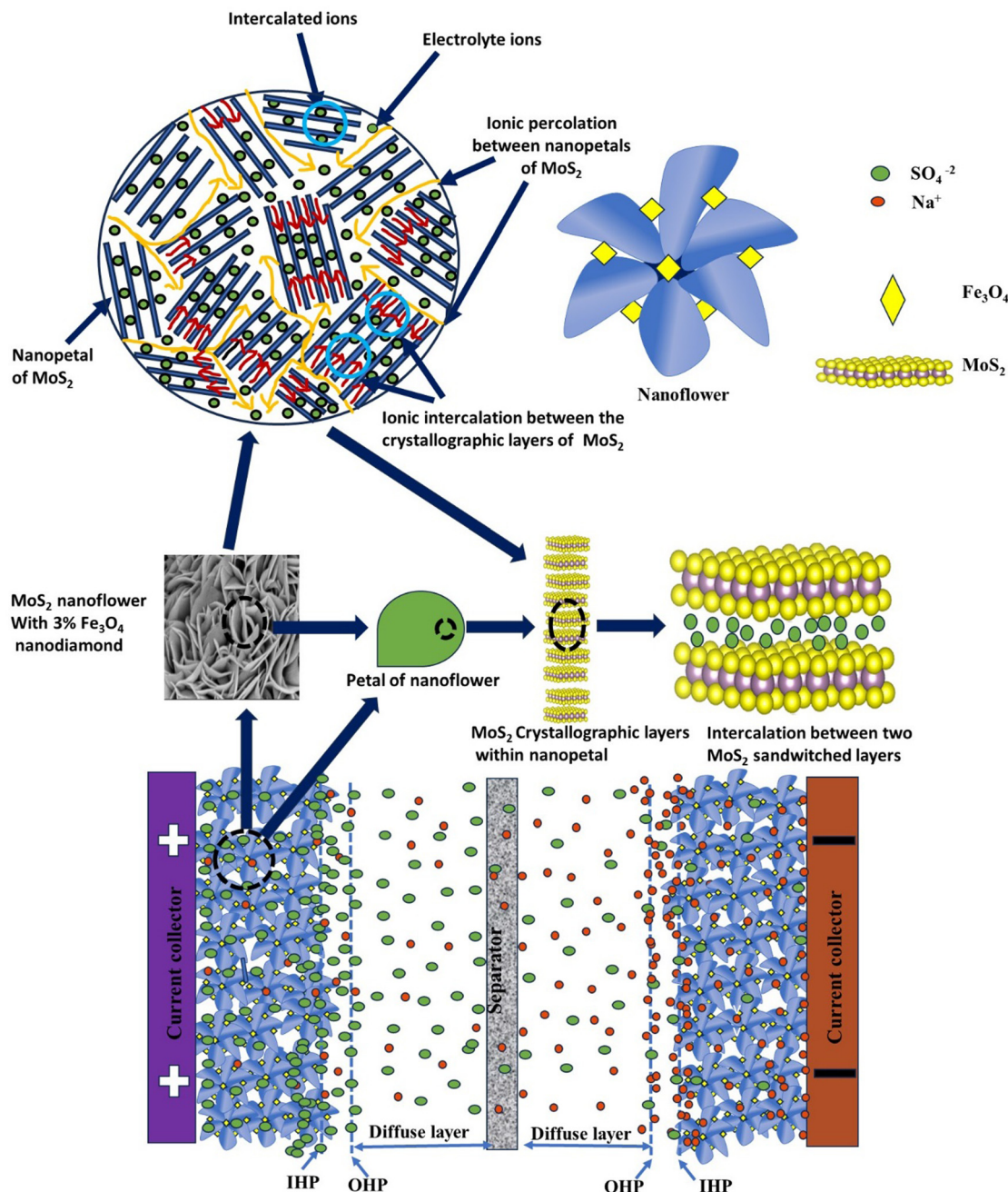
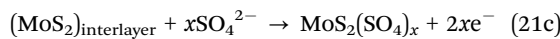
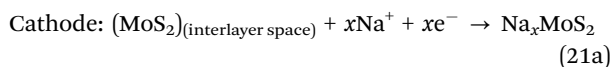


**Fig. 13** A schematic representation of the charge storage mechanism of a two-electrode symmetric supercapacitor. Under an applied voltage,  $\text{Na}^+$  and  $\text{SO}_4^{2-}$  ions migrate toward the respective electrodes, forming two distinct regions: the inner Helmholtz plane (IHP), which is located directly adjacent to the electrode surface, and the outer Helmholtz plane (OHP), which extends further into the bulk electrolyte. The interaction between these planes establishes the basis of the electric double layer capacitance (EDLC). Additionally, the porous, defect-rich structure with slightly widened interlayer spacing of the  $\text{MoS}_2$ /(3%)  $\text{Fe}_3\text{O}_4$  electrode provides better electrode–electrolyte interaction, enhancing the charge storage capacity through processes like ion percolation and intercalation, surface adsorption, and redox reactions. These mechanisms contribute significantly to the pseudocapacitance of the system. The combination of EDLC and pseudocapacitance mechanisms underpins the overall charge storage process, allowing for enhanced energy storage performance.



Reversible surface redox reactions have a great influence on the overall charge storage process. The vacancy defects could create under-coordinated atoms around the defect site, which are chemically more active. These atoms can strongly interact

with reactants, making the surface more reactive for redox processes. Vacancies alter the local electronic density of states, often creating localized defect states. These can lower the activation energy for electron transfer during redox reactions, enhancing the reaction rate. Additionally, the diffuse layer facilitates the necessary conditions for these surface redox reactions by providing a stable ionic environment that supports

fast and reversible processes at the electrode surfaces. Consequently, the total capacitance is derived from the combined contributions of both electric double-layer capacitance (EDLC) and pseudocapacitance mechanisms, enhancing the overall energy storage capability.

However, the charging process is reversed during discharging. When the potential applied to the electrode is reduced

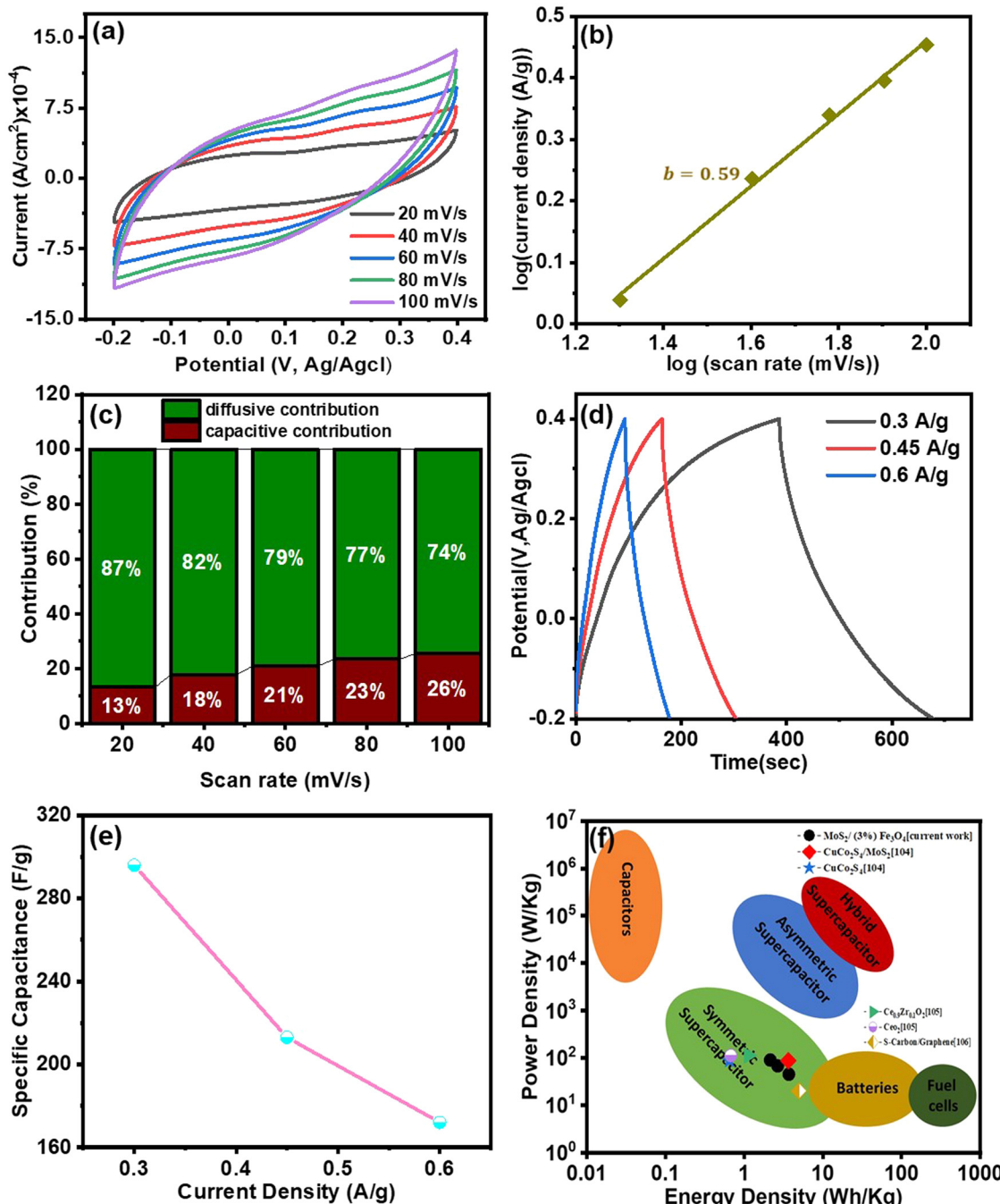


**Fig. 14** Electrochemical performance of a symmetrical two electrode system: (a) CV loops at various scan rates ranging from  $20 \text{ mV s}^{-1}$  to  $50 \text{ mV s}^{-1}$ ; (b) Tafel's slope indicates the charge storage mechanism to be a combination of EDLC and pseudocapacitive processes; (c) variation in the diffusion and capacitive contribution ratio as a function of scan rate; (d) GCD curves at different current densities; (e) variation of specific capacitance as a function of current density; and (f) Ragone plot showing the energy and power densities of symmetric supercapacitors based on various electrode materials. Each colored data point represents a specific material reported in recent supercapacitor research.



during the discharging process, the  $\text{Na}^+$  and  $\text{SO}_4^{2-}$  ions that were previously intercalated into the  $\text{MoS}_2/(3\%) \text{Fe}_3\text{O}_4$  lattice and participated in the surface redox reactions are released back into the electrolyte solution, which can be shown simply by reversing eqn (20) and (21), associated with a reverse redox reaction, deintercalation and surface desorption processes.

Now, the electrochemical measurements with two electrode configuration (in Fig. 14) were performed within the same potential window ( $-0.2$  to  $0.6$  V) adopted for the three-electrode system. The measurements were carried out at different scan rates ranging from  $20$  to  $100$   $\text{mV s}^{-1}$  in a  $0.5$  M  $\text{Na}_2\text{SO}_4$  aqueous electrolyte. The CV loops of the  $\text{MoS}_2/(3\%) \text{Fe}_3\text{O}_4$  electrode, as shown in Fig. 14(a), maintained their shape even at high scan rates, indicating the material's excellent reversibility and high-rate capability in the case of two electrode device application. The CV loops of the  $\text{MoS}_2/(3\%) \text{Fe}_3\text{O}_4$  material exhibit a consistently stable quasi-rectangular shape across the entire potential range, regardless of the scan rate, indicating that the mechanisms of both electric double-layer capacitance (EDLC) and pseudocapacitance may be active in the charge storage process.<sup>69</sup> Additionally, in order to understand the charge storage mechanism of the electrodes, the value of Tafel slope ' $b$ ' (according to eqn (10)) was calculated, which was found to be  $0.59$  as shown in Fig. 14(b). The value is comparable to those observed for the three-electrode system, suggesting a charge storage mechanism that combines both the faradaic and the capacitive processes. To comprehend the reaction kinetics, both capacitive and diffusive current contributions were determined as shown in Fig. 14(c) following eqn (16). The figure demonstrates that as the scan rate increases, the capacitive contribution of the synthesized samples increases, while the diffusion contribution decreases. At  $100$   $\text{mV s}^{-1}$ , the diffusive and capacitive current contributions are  $74\%$  and  $26\%$  respectively, illustrating a balance between these two contributions. This balance is crucial for understanding the electrochemical mechanisms and optimizing the performance of supercapacitor devices.

GCD measurements were conducted to determine the specific capacitance, as well as the power and energy densities of the synthesized materials under two electrode configuration. The following equations were used to calculate the specific capacitance ( $C_{\text{sp}}$ ) of a single electrode, along with the energy density ( $E$ ) and power density ( $P$ ) of the two-electrode system:

$$C_{\text{sp}} (\text{F g}^{-1}) = \frac{2 \times I \times \Delta t}{m \times \Delta V} \quad (22)$$

$$E (\text{W h kg}^{-1}) = \frac{C_{\text{sp}} \times (\Delta V)^2 \times 1000}{8 \times 3600} \quad (23)$$

$$P (\text{W kg}^{-1}) = \frac{E \times 1000}{\Delta t} \quad (24)$$

Fig. 14(d) shows the charging and discharging curves for  $\text{MoS}_2/(3\%) \text{Fe}_3\text{O}_4$  nanocomposite electrodes at various current densities, from which the specific capacitance values were determined and it can be found that they decrease with the

increase in current density, as shown in Fig. 14(e). The maximum capacitance observed is  $296 \text{ F g}^{-1}$  at a current density of  $0.3 \text{ A g}^{-1}$ . The operational efficiency of energy storage devices is critically influenced by their energy density ( $E$ ) and power density ( $P$ ). The Ragone plot in Fig. 14(f) illustrates the energy and power densities of various reported supercapacitor systems, with each data point representing a distinct electrode configuration. The  $\text{CuCo}_2\text{S}_4-\text{MoS}_2$  composite (red diamond) exhibits an energy density of  $\sim 3.65 \text{ W h kg}^{-1}$  and a power density of  $\sim 87 \text{ W kg}^{-1}$ .<sup>104</sup> In comparison,  $\text{CuCo}_2\text{S}_4$  (blue star) displays a significantly lower energy density ( $\sim 0.65 \text{ W h kg}^{-1}$ ) while maintaining a comparable power density.<sup>5</sup> The  $\text{Ce}_{0.9}\text{Zr}_{0.1}\text{O}_2$  electrode (green triangle) achieves an energy density of  $\sim 1.13 \text{ W h kg}^{-1}$  and a power density of  $\sim 112.5 \text{ W kg}^{-1}$ , while  $\text{CeO}_2$  (purple circle) shows slightly lower energy ( $\sim 0.68 \text{ W h kg}^{-1}$ ) at the same power level.<sup>105</sup> Notably, the sulfur-doped carbon and graphene composite (yellow diamond) delivers a relatively high energy density of  $\sim 5 \text{ W h kg}^{-1}$  at a power density of  $\sim 20 \text{ W kg}^{-1}$ .<sup>106</sup> The  $\text{MoS}_2/(3\%) \text{Fe}_3\text{O}_4$  composite investigated in this study, represented by black dotted markers, demonstrates energy densities of  $3.7$ ,  $2.67$ , and  $2.15 \text{ W h kg}^{-1}$  at corresponding power densities of  $45$ ,  $67.5$ , and  $90 \text{ W kg}^{-1}$  and these points very closely resemble the obtained results from the present-day studies and reflect the efficient performance level of various symmetric systems. Therefore, the improved performance of the  $\text{MoS}_2/(3\%) \text{Fe}_3\text{O}_4$  electrode provides strong evidence for the material's supercapacitive capabilities.

Finally, we have fabricated a coin cell device using the optimized  $\text{MoS}_2/(3\%) \text{Fe}_3\text{O}_4$  nanocomposite electrode as shown in Fig. SF5 (ESI†). To showcase its practical utility, the device was successfully employed to power an LED lamp. A series of six photographs have been included for illustration: the first image captures the moment the lamp is initially turned on, while the subsequent images display the lamp remaining continuously illuminated at  $30$ ,  $60$ ,  $90$ ,  $120$ , and  $150$  seconds, respectively. This demonstration clearly reflects the reasonably good energy storage and delivery capabilities of the  $\text{MoS}_2-(3\%) \text{Fe}_3\text{O}_4$  nanocomposite-based device.

## Conclusion

In this work, pristine  $\text{MoS}_2$  and  $1-5 \text{ wt\%}$   $\text{Fe}_3\text{O}_4$  nanodiamond incorporated  $\text{MoS}_2$  nanoflowers were synthesized by a simple hydrothermal route to evaluate and optimize the amounts of the two nanostructured components in the nanocomposite that would deliver an optimized electrochemical performance for high performance supercapacitor electrodes. The XRD analysis confirms the successful formation of the desired material, with the highest level of crystallographic defect induced disorders for an optimum combination of  $3 \text{ wt\%}$   $\text{Fe}_3\text{O}_4$  incorporated  $\text{MoS}_2$  nanocomposite. The SEM micrographs revealed distinct morphological changes leading to fragmentation and random piling up of  $\text{MoS}_2$  nanopetals hampering the radial alignment of the petal like formations at higher  $\text{Fe}_3\text{O}_4$  content. TEM analysis revealed that the nanostructured composite maintains a hierarchical structure, with the interlayer spacing of  $\text{MoS}_2$



increased by ~10% for an increase in  $\text{Fe}_3\text{O}_4$  content from 0 to 3 wt%, which is followed by a sudden drop in the spacing beyond the given composition limit. The comprehensive crystallographic and morphological analyses predicted a superior electrochemical performance of the nanocomposite with 3 wt%  $\text{Fe}_3\text{O}_4$  compared to other synthesized nanostructured materials. In a three-electrode system, the  $\text{MoS}_2$ /(3%)  $\text{Fe}_3\text{O}_4$  nanocomposite electrode demonstrated an impressive specific capacitance of  $712 \text{ F g}^{-1}$  at  $0.3 \text{ A g}^{-1}$ , along with excellent cyclic stability, retaining 84% of its initial capacitance after 10 000 cycles. The incorporation of  $\text{Fe}_3\text{O}_4$  nanodiamonds significantly boosted the electrochemical performance of  $\text{MoS}_2$  nanoflowers through the formation of a defect-rich crystal structure, providing more active sites and allowing a greater number of electrolyte ions to interact with both the outer surface and nanoporous interior of the composite. The increased interlayer spacing with  $\text{Fe}_3\text{O}_4$  nanodiamond incorporation allowed more efficient penetration of electrolyte ions into the electrode materials enhancing the overall capacitive response of the  $\text{MoS}_2$ / $\text{Fe}_3\text{O}_4$  nanocomposite. The electrochemical performance of the nanostructured composite reached its maximum at 3 wt% of  $\text{Fe}_3\text{O}_4$  nanodiamonds. The lowest charge transfer resistance observed for this composition significantly contributed towards a more efficient faradaic process, enhancing the specific capacitance. With further incorporation of  $\text{Fe}_3\text{O}_4$  (5 wt%) beyond this limit, excess nanodiamonds hindered the uninterrupted growth of  $\text{MoS}_2$  nano-petals causing the nanoporous channels for electrolytic ions to collapse along with a reduction in  $\text{MoS}_2$  interlayer spacing, restricting the electrode/electrolyte interface area and the ionic intercalation/deintercalation process. In the case of a two electrode system with the optimized composition mimicking the real devices, the charge storage mechanism involved both capacitive and faradaic processes similar to the three-electrode counterpart. The kinetics study of the optimized nanocomposite showed certain balance between capacitive and diffusive contributions of current, which is crucial for device optimization. The energy and the power densities of the optimized nanocomposite were found to fall within the region of symmetric supercapacitors in the Ragone plot. Consequently, the  $\text{MoS}_2$ /(3%)  $\text{Fe}_3\text{O}_4$  nanocomposite emerged as the optimal combination, outperforming a plethora of nanocomposites in terms of electrochemical responses, reinforcing its effectiveness as a high-performance supercapacitor electrode material.

## Author contributions

Md. Raihan Siddiki: conceptualization, methodology, investigation, formal analysis, writing – original draft. Shahid Abubakar Abtahee: conceptualization, methodology, investigation, formal analysis. Mehedi Hasan: investigation, formal analysis. Mizanur Rahaman: investigation, formal analysis. Muhammad Rakibul Islam: investigation, formal analysis. Md. Abdullah Zubair: supervision, conceptualization, methodology, investigation, writing – review & editing.

## Conflicts of interest

There are no conflicts to declare.

## Data availability

All necessary data are available within this article.

## Acknowledgements

The authors are grateful to the Department of Nanomaterials and Ceramic Engineering and the Department of Physics, BUET, for their support in synthesis and characterization of the materials. We also acknowledge the Committee for Advanced Studies and Research (CASR), BUET, for financial support.

## References

- 1 P. Simon and Y. Gogotsi, *Nat. Mater.*, 2008, **7**, 845–854.
- 2 T. Zhu, J. Pan, Z. An, R. Zhe, Q. Ou and H.-E. Wang, *J. Mater. Chem. A*, 2022, **10**, 20375–20385.
- 3 P.-Y. Liu, J.-J. Zhao, Z.-P. Dong, Z.-L. Liu and Y.-Q. Wang, *J. Alloys Compd.*, 2021, **854**, 157181.
- 4 H. Lu and X. S. Zhao, *Sustainable Energy Fuels*, 2017, **1**, 1265–1281.
- 5 Md. R. Islam, M. Rahaman, Md. M. Billah and M. R. Islam, *Mater. Adv.*, 2024, **5**, 5307–5321.
- 6 Y.-F. Ren, Z.-L. He, H.-Z. Zhao and T. Zhu, *Rare Met.*, 2022, **41**, 830–835.
- 7 D. Lan, Y. Chen, P. Chen, X. Chen, X. Wu, X. Pu, Y. Zeng and Z. Zhu, *ACS Appl. Mater. Interfaces*, 2014, **6**, 11839–11845.
- 8 W. Gu and G. Yushin, *Wiley Interdiscip. Rev.: Energy Environ.*, 2014, **3**, 424–473.
- 9 P. Thounthong, V. Chunkag, P. Sethakul, S. Sikkabut, S. Pierfederici and B. Davat, *J. Power Sources*, 2011, **196**, 313–324.
- 10 Y. Dong, Y. Wang, Y. Xu, C. Chen, Y. Wang, L. Jiao and H. Yuan, *Electrochim. Acta*, 2017, **225**, 39–46.
- 11 X. Xiao, G. Zhang, Y. Xu, H. Zhang, X. Guo, Y. Liu and H. Pang, *J. Mater. Chem. A*, 2019, **7**, 17266–17271.
- 12 X. Guo, Y.-Z. Zhang, F. Zhang, Q. Li, D. H. Anjum, H. Liang, Y. Liu, C. Liu, H. N. Alshareef and H. Pang, *J. Mater. Chem. A*, 2019, **7**, 15969–15974.
- 13 J. Ma, X. Guo, Y. Yan, H. Xue and H. Pang, *Adv. Sci.*, 2018, **5**, 1700986.
- 14 J. Shin, D. Shin, H. Hwang, T. Yeo, S. Park and W. Choi, *J. Mater. Chem. A*, 2017, **5**, 13488–13498.
- 15 A. Zhang, R. Zhao, L. Hu, R. Yang, S. Yao, S. Wang, Z. Yang and Y. Yan, *Adv. Energy Mater.*, 2021, **11**, 2101412.
- 16 Y.-P. Zhu, C. Xia, Y. Lei, N. Singh, U. Schwingenschlögl and H. N. Alshareef, *Nano Energy*, 2019, **56**, 357–364.
- 17 W. Li, J. Shao, Q. Liu, X. Liu, X. Zhou and J. Hu, *Electrochim. Acta*, 2015, **157**, 108–114.



18 W. Lu, Y. Li, M. Yang, X. Jiang, Y. Zhang and Y. Xing, *ACS Appl. Energy Mater.*, 2020, **3**, 8190–8197.

19 C. Zhang, Z. Peng, Y. Chen, H. Chen, B. Zhang, H. Cheng, J. Wang and M. Deng, *Electrochim. Acta*, 2020, **347**, 136246.

20 X. Chia, A. Y. S. Eng, A. Ambrosi, S. M. Tan and M. Pumera, *Chem. Rev.*, 2015, **115**, 11941–11966.

21 R. N. Bulakhe, V. H. Nguyen and J.-J. Shim, *New J. Chem.*, 2017, **41**, 1473–1482.

22 N. Choudhary, M. R. Islam, N. Kang, L. Tetard, Y. Jung and S. I. Khondaker, *J. Phys.: Condens. Matter*, 2016, **28**, 364002.

23 M. Chen, Y. Dai, J. Wang, Q. Wang, Y. Wang, X. Cheng and X. Yan, *J. Alloys Compd.*, 2017, **696**, 900–906.

24 F. Ghasemi, M. Jalali, A. Abdollahi, S. Mohammadi, Z. Sanaee and S. Mohajerzadeh, *RSC Adv.*, 2017, **7**, 52772–52781.

25 X. Huang, Z. Zeng and H. Zhang, *Chem. Soc. Rev.*, 2013, **42**, 1934.

26 C. Sha, B. Lu, H. Mao, J. Cheng, X. Pan, J. Lu and Z. Ye, *Carbon*, 2016, **99**, 26–34.

27 Y. Zhang, T. He, G. Liu, L. Zu and J. Yang, *Nanoscale*, 2017, **9**, 10059–10066.

28 X. Zhou, L.-J. Wan and Y.-G. Guo, *Nanoscale*, 2012, **4**, 5868.

29 J. B. Cook, H. Kim, Y. Yan, J. S. Ko, S. Robbennolt, B. Dunn and S. H. Tolbert, *Adv. Energy Mater.*, 2016, **6**, 1501937.

30 M. H. Ahmad, R. B. Alam, A. Ul-Hamid, S. F. U. Farhad and M. R. Islam, *J. Energy Storage*, 2022, **47**, 103551.

31 Md. R. Islam, M. Rahaman, Md. M. Billah and M. R. Islam, *Mater. Adv.*, 2024, **5**, 5307–5321.

32 M. Rahaman, M. J. Islam, A. Ul-Hamid and M. R. Islam, *Surf. Interfaces*, 2024, **45**, 103886.

33 P. Bayat, K. Karami, F. Tavakoli, S. Rahimi, S. Kamali and B. Rezaei, 2023, preprint, DOI: [10.21203/rs.3.rs-3354348/v1](https://doi.org/10.21203/rs.3.rs-3354348/v1).

34 P. Salarizadeh, M. B. Askari, K. Hooshyari and H. Saeidfirozeh, *Nanotechnology*, 2020, **31**, 435401.

35 Z. Li, Y. Zhang and W. Zhang, *Mater. Res. Express*, 2017, **4**, 055018.

36 M. Sarno and A. Troisi, *J. Nanosci. Nanotechnol.*, 2017, **17**, 3735–3743.

37 G. Yu, L. Hu, N. Liu, H. Wang, M. Vosqueritchian, Y. Yang, Y. Cui and Z. Bao, *Nano Lett.*, 2011, **11**, 4438–4442.

38 X. Li, L. Zhang, X. Zang, X. Li and H. Zhu, *ACS Appl. Mater. Interfaces*, 2016, **8**, 10866–10873.

39 A. Gigot, M. Fontana, M. Serrapede, M. Castellino, S. Bianco, M. Armandi, B. Bonelli, C. F. Pirri, E. Tresso and P. Rivolo, *ACS Appl. Mater. Interfaces*, 2016, **8**, 32842–32852.

40 L. Hu, Y. Ren, H. Yang and Q. Xu, *ACS Appl. Mater. Interfaces*, 2014, **6**, 14644–14652.

41 S. Dutta and S. De, *Mater. Today: Proc.*, 2018, **5**, 9771–9775.

42 H. Song, A. Tang, G. Xu, L. Liu, Y. Pan and M. Yin, *Int. J. Electrochem. Sci.*, 2018, **13**, 6708–6716.

43 N. Torres-Gómez, O. Nava, L. Argueta-Figueroa, R. García-Contreras, A. Baeza-Barrera and A. R. Vilchis-Nestor, *J. Nanomater.*, 2019, **2019**, 1–15.

44 Md. A. Zubair, T. Moura and M. T. Chowdhury, *Phys. Chem. Chem. Phys.*, 2023, **25**, 27628–27653.

45 Z. Wu, B. Li, Y. Xue, J. Li, Y. Zhang and F. Gao, *J. Mater. Chem. A*, 2015, **3**, 19445–19454.

46 X. Li, T. Li, Y. Ma, Q. Wei, W. Qiu, H. Guo, X. Shi, P. Zhang, A. M. Asiri, L. Chen, B. Tang and X. Sun, *Adv. Energy Mater.*, 2018, **8**, 1801357.

47 A. A. Pawar, H. A. Bandal and H. Kim, *J. Alloys Compd.*, 2021, **863**, 158742.

48 N. Esfandiari, M. Kashefi, M. Mirjalili and S. Afsharnezhad, *Mater. Sci. Eng. B*, 2020, **262**, 114690.

49 Md. R. Siddiki, S. A. Abtahee, M. Rahaman, M. R. Islam and Md. A. Zubair, *Mater. Adv.*, 2024, **5**, 9641–9655.

50 L. Ma, L. Xu, X. Xu, X. Zhou, J. Luo and L. Zhang, *Mater. Sci. Eng. B*, 2016, **212**, 30–38.

51 G. Tang, Y. Wang, W. Chen, H. Tang and C. Li, *Mater. Lett.*, 2013, **100**, 15–18.

52 R. Zhou, C. Han and X. Wang, *J. Power Sources*, 2017, **352**, 99–110.

53 A. M. Alsaad, A. A. Ahmad, Q. M. Al-Bataineh, A. A. Bani-Salameh, H. S. Abdullah, I. A. Qattan, Z. M. Albataineh and A. D. Telfah, *Materials*, 2020, **13**, 1737.

54 M. Fang, G. Dong, R. Wei and J. C. Ho, *Adv. Energy Mater.*, 2017, **7**, 1700559.

55 R. Sha, A. Gopalakrishnan, K. V. Sreenivasulu, V. V. S. S. Srikanth and S. Badhulika, *J. Alloys Compd.*, 2019, **794**, 26–34.

56 P. Bayat, K. Karami, M. Gholamian, F. Tavakoli, S. Rahimi, S. Kamali and B. Rezaei, *ChemistrySelect*, 2024, **9**, e202304049.

57 Y. Zhao, W. Cai, Y. Shi, J. Tang, Y. Gong, M. Chen and Q. Zhong, *ACS Sustainable Chem. Eng.*, 2020, **8**, 12603–12611.

58 S. Wei, R. Zhou and G. Wang, *ACS Omega*, 2019, **4**, 15780–15788.

59 X. Wang, J. Ding, S. Yao, X. Wu, Q. Feng, Z. Wang and B. Geng, *J. Mater. Chem. A*, 2014, **2**, 15958–15963.

60 Z. Hu, L. Wang, K. Zhang, J. Wang, F. Cheng, Z. Tao and J. Chen, *Angew. Chem.*, 2014, **126**, 13008–13012.

61 K. Ramakrishnan, C. Nithya and R. Karvembu, *Nanoscale Adv.*, 2019, **1**, 334–341.

62 J. Xie, H. Zhang, S. Li, R. Wang, X. Sun, M. Zhou, J. Zhou, X. W. (David) Lou and Y. Xie, *Adv. Mater.*, 2013, **25**, 5807–5813.

63 J. Xie, J. Zhang, S. Li, F. Grote, X. Zhang, H. Zhang, R. Wang, Y. Lei, B. Pan and Y. Xie, *J. Am. Chem. Soc.*, 2013, **135**, 17881–17888.

64 Y. Sun, Q. Liu, S. Gao, H. Cheng, F. Lei, Z. Sun, Y. Jiang, H. Su, S. Wei and Y. Xie, *Nat. Commun.*, 2013, **4**, 2899.

65 K. D. Rasamani, F. Alimohammadi and Y. Sun, *Mater. Today*, 2017, **20**, 83–91.

66 N. Kanaujiya, N. Kumar, A. K. Srivastava, Y. Sharma and G. D. Varma, *J. Electroanal. Chem.*, 2018, **824**, 226–237.

67 J. Wang, H. Zhou, M. Zhu, A. Yuan and X. Shen, *J. Alloys Compd.*, 2018, **744**, 220–227.

68 R. Zhou, S. Wei, Y. Liu, N. Gao, G. Wang, J. Lian and Q. Jiang, *Sci. Rep.*, 2019, **9**, 3980.

69 G. K. Sharma, B. Ranjan and D. Kaur, *Appl. Phys. Lett.*, 2021, **118**, 203901.

70 R. Wang, S. Wang, X. Peng, Y. Zhang, D. Jin, P. K. Chu and L. Zhang, *ACS Appl. Mater. Interfaces*, 2017, **9**, 32745–32755.



71 B. A. Ali, A. M. A. Omar, A. S. G. Khalil and N. K. Allam, *ACS Appl. Mater. Interfaces*, 2019, **11**, 33955–33965.

72 M. R. Siddiki, S. A. Abtahee and M. A. Zubair, in *Comprehensive Materials Processing*, Elsevier, 2024, pp. 340–379.

73 T. Xiong, W. S. V. Lee and J. Xue, *ACS Appl. Energy Mater.*, 2018, **1**, 5619–5626.

74 B. A. Ali, O. I. Metwalli, A. S. G. Khalil and N. K. Allam, *ACS Omega*, 2018, **3**, 16301–16308.

75 S.-L. Kuo, J.-F. Lee and N.-L. Wu, *J. Electrochem. Soc.*, 2006, **154**, A34.

76 S. K. Ghosh, *ACS Omega*, 2020, **5**, 25493–25504.

77 J. Zhu, S. Tang, H. Xie, Y. Dai and X. Meng, *ACS Appl. Mater. Interfaces*, 2014, **6**, 17637–17646.

78 L. Xu, G. Pan, C. Yu, J. Li, Z. Gong, T. Lu and L. Pan, *Inorg. Chem. Front.*, 2023, **10**, 1748–1757.

79 L. Chen, X. Xu, L. Wan, G. Zhu, Y. Li, T. Lu, M. D. Albaqami, L. Pan and Y. Yamauchi, *Mater. Chem. Front.*, 2021, **5**, 3480–3488.

80 M. Tarek and M. A. Basith, *J. Mater. Chem. C*, 2023, **11**, 16605–16622.

81 Y. Liu, S. P. Jiang and Z. Shao, *Mater. Today Adv.*, 2020, **7**, 100072.

82 Y. Wang, Z. Shi, Y. Huang, Y. Ma, C. Wang, M. Chen and Y. Chen, *J. Phys. Chem. C*, 2009, **113**, 13103–13107.

83 M. Toupin, T. Brousse and D. Bélanger, *Chem. Mater.*, 2002, **14**, 3946–3952.

84 X.-L. Bai, Y.-L. Gao, Z.-Y. Gao, J.-Y. Ma, X.-L. Tong, H.-B. Sun and J. A. Wang, *Appl. Phys. Lett.*, 2020, **117**, 183901.

85 Y. Chen, W. Ma, K. Cai, X. Yang and C. Huang, *Electrochim. Acta*, 2017, **246**, 615–624.

86 A. K. Thakur, A. B. Deshmukh, R. B. Choudhary, I. Karbhal, M. Majumder and M. V. Shelke, *Mater. Sci. Eng. B*, 2017, **223**, 24–34.

87 S. Guo, W. Chen, M. Li, J. Wang, F. Liu and J. P. Cheng, *Electrochim. Acta*, 2018, **271**, 498–506.

88 J.-H. Lin, *Materials*, 2018, **11**, 263.

89 S. S. Nardekar, K. Krishnamoorthy, P. Pazhamalai, S. Sahoo, V. K. Mariappan and S.-J. Kim, *J. Mater. Chem. A*, 2020, **8**, 13121–13131.

90 Z. Yu, L. Tetard, L. Zhai and J. Thomas, *Energy Environ. Sci.*, 2015, **8**, 702–730.

91 M. A. A. Mohd Abdah, N. A. Zubair, N. H. N. Azman and Y. Sulaiman, *Mater. Chem. Phys.*, 2017, **192**, 161–169.

92 M. Gaire, K. Liang, S. Luo, B. Subedi, S. Adireddy, K. Schroder, S. Farnsworth and D. B. Chrisey, *RSC Adv.*, 2020, **10**, 16817–16825.

93 S. Grenier, G. Subías, J. García, J. Blasco and L. Morellón, *Phys. Rev. B*, 2018, **97**, 104403.

94 M. D. Nguyen, H.-V. Tran, S. Xu and T. R. Lee, *Appl. Sci.*, 2021, **11**, 11301.

95 Y. Liu, D. He, H. Wu, J. Duan and Y. Zhang, *Electrochim. Acta*, 2015, **164**, 154–162.

96 P. Si, S. Ding, X.-W. (David) Lou and D.-H. Kim, *RSC Adv.*, 2011, **1**, 1271.

97 F. Wang, K. Zhou, J. Zheng and J. Ma, *Synth. Met.*, 2019, **256**, 116113.

98 Z. Ling, Z. Wang, M. Zhang, C. Yu, G. Wang, Y. Dong, S. Liu, Y. Wang and J. Qiu, *Adv. Funct. Mater.*, 2016, **26**, 111–119.

99 K. Xu, S. Li, J. Yang, H. Xu and J. Hu, *J. Alloys Compd.*, 2016, **678**, 120–125.

100 J. Li, Y. Chen, Q. Wu and H. Xu, *J. Alloys Compd.*, 2017, **693**, 373–380.

101 H. Jiang, Y. Dai, Y. Hu, W. Chen and C. Li, *ACS Sustainable Chem. Eng.*, 2014, **2**, 70–74.

102 Y. Xiong, M. Zhou, H. Chen, L. Feng, Z. Wang, X. Yan and S. Guan, *Appl. Surf. Sci.*, 2015, **357**, 1024–1030.

103 G. Han, Y. Liu, E. Kan, J. Tang, L. Zhang, H. Wang and W. Tang, *RSC Adv.*, 2014, **4**, 9898–9904; Y. Liu, D. He, H. Wu, J. Duan and Y. Zhang, *Electrochim. Acta*, 2015, **164**, 154–162.

104 S. Hasan, A. H. Reaz, S. Das, C. K. Roy and M. M. Basith, *J. Mater. Chem. C*, 2022, **10**, 7980–7996.

105 S. Ghosh, G. R. Rao and T. Thomas, *arXiv*, 2021, preprint, arXiv:2101.02907, DOI: [10.48550/arXiv.2101.02907](https://doi.org/10.48550/arXiv.2101.02907).

106 M. Seredych and T. J. Bandosz, *J. Mater. Chem. A*, 2013, **1**, 11717–11727.

